Redox Biology 67 (2023) 102922

Contents lists available at ScienceDirect

Redox Biology

journal homepage: www.elsevier.com/locate/redox

Tobacco toxins induce osteoporosis through ferroptosis

Zheng Jing [a,b,c], Yuzhou Li [a,b,c], He Zhang [a,b,c], Tao Chen [a], Jinrui Yu [a], Xinxin Xu [a], Yulong Zou [d], Xu Wang [a], Kai Xiang [a], Xuerui Gong [a], Ping He [a], Yiru Fu [a], Mingxing Ren [a], Ping Ji [a,b,c,**], Sheng Yang [a,b,c,*]

[a] Stomatological Hospital of Chongqing Medical University, Chongqing, China
[b] Chongqing Key Laboratory of Oral Diseases and Biomedical Sciences, Chongqing, China
[c] Chongqing Municipal Key Laboratory of Oral Biomedical Engineering of Higher Education, Chongqing, China
[d] Department of Orthopedics, Second Affiliated Hospital of Chongqing Medical University, China

ARTICLE INFO

Keywords:
Ferroptosis
Ferritinophagy
Osteoporosis
Cigarette smoke extract
Bone marrow mesenchymal stem cells

ABSTRACT

Clinical epidemiological studies have confirmed that tobacco smoking disrupts bone homeostasis and is an independent risk factor for the development of osteoporosis. The low viability and inferior osteogenic differentiation of bone marrow mesenchymal stem cells (BMSCs) are important etiologies of osteoporosis. However, few basic studies have elucidated the specific mechanisms that tobacco toxins devastated BMSCs and consequently induced or exacerbated osteoporosis. Herein, our clinical data showed the bone mineral density (BMD) values of femoral neck in smokers were significantly lower than non-smokers, meanwhile cigarette smoke extract (CSE) exposure led to a significant decrease of BMD in rats and dysfunction of rat BMSCs (rBMSCs). Transcriptomic analysis and phenotype experiments suggested that the ferroptosis pathway was significantly activated in CSE-treated rBMSCs. Accumulated intracellular reactive oxygen species activated AMPK signaling, furtherly promoted NCOA4-mediated ferritin-selective autophagic processes, increased labial iron pool and lipid peroxidation deposition, and ultimately led to ferroptosis in rBMSCs. Importantly, in vivo utilization of ferroptosis and ferritinophagy inhibitors significantly alleviated BMD loss in CSE-exposed rats. Our study innovatively reveals the key mechanism of smoking-related osteoporosis, and provides a possible route targeting on the perspective of BMSC ferroptosis for future prevention and treatment of smoking-related bone homeostasis imbalance.

1. Introduction

Tobacco smoking, as one of the most common unhealthy behaviors and the leading cause of preventable death across the world, has been confirmed as an independent risk factor for the progression of osteoporosis [1–5]. Bone tissue undergoes uninterrupted remodeling at all stages of life, which is dependent on balanced bone turnover regulated by osteoblasts-mediated bone formation and osteoclasts-mediated bone resorption [6,7]. Tobacco toxins enters and accumulates in human body that interferes this dynamic equilibrium process, resulting in decreased osteogenesis in osteoblasts and/or enhanced resorption in osteoclasts, and ultimately lead to osteoporosis characterized by reduced bone mass, deteriorated bone structure and increased bone fragility [8]. However, the specific molecular mechanism underlying the imbalance of bone turnover caused by tobacco toxins remains unclear, and it is essential and urgent to find effective interventions for smokers toprevent bone destruction and resolve related clinical problems.

Bone marrow mesenchymal stem cells (BMSCs) can differentiate into osteoblasts and regulate the function of osteoclasts, which plays a crucial role in maintaining the dynamic balance of bone metabolism [9]. Importantly, damaged BMSCs will lead to osteoporosis. Frequent exposure to cigarette smoke extract (CSE) induces intracellular reactive oxygen species (ROS) accumulation that causes senescence, apoptosis and depletion of BMSCs, along with disorder of intracellular ion metabolism, such as decreased calcium influx, iron complex generation and zinc overflow etc [7,10–13]. Particularly, iron is an essential trace element in regulating the redox chemistry and homeostasis in organisms, and optimal iron levels is essential for balanced bone homeostasis that either overload or deficiency of iron is associated with weakened bones [14]. Recent findings have drawn our attention to iron homeostasis imbalance as potential indicator to explain the toxic mechanism of tobacco toxins

* Corresponding author. Stomatological hospital of Chongqing Medical University , 426 Songshi North Road, Yubei District, Chongqing, 401147, China.
** Corresponding author. Chongqing Key Laboratory of Oral Diseases and Biomedical Sciences, Chongqing, China.
E-mail address: 500283@cqmu.edu.cn (S. Yang).

https://doi.org/10.1016/j.redox.2023.102922
Received 5 September 2023; Received in revised form 27 September 2023; Accepted 3 October 2023
Available online 4 October 2023

Abbreviations

3-MA	3-methyladenine
4-HNE	4-hydroxynonenal
AMPK	AMP-activated protein kinase
BafA1	Bafilomycin A1
BV/TV	Bone volume/tissue volume
rBMSCs	Rat bone marrow mesenchymal stem cells
rBMMs	Rat bone marrow mononuclear macrophages
CSE	Cigarette smoke extract
CQ	Chloroquine
Col-1	Collagen I
DFO	Deferoxamine mesylate salt
Fer-1	Ferrostatin-1
GPx4	Glutathione peroxidase 4
GSH	Glutathione
LC3	Microtubule associated protein 1 light chain 3
MDA	Malondialdehyde
mTOR	mammalian target of rapamycin
NCOA4	Nuclear receptor coactivator 4
PGSK	Phen Green™ SK
p62	SQSTM1 sequestosome 1
ROS	Reactive oxygen species
RAPA	Rapamycin
siRNA	Small interfering RNA
TEM	Transmission electron microscopy
Tb.Th	Trabecular thickness
Tb.N	Trabecular number
Tb.Sp	Trabecular separation
TRAP	Tartrateresistant acid phosphatase
TMRE	Tetramethylrhodamine, ethyl ester
ULK1	Unc-51 like autophagy activating kinase 1

[15]. Oxygen-containing functional groups (e.g., carboxylates, esters, and phenolic hydroxides) produce from cigarette smoke undergo proton dissociation at physiological pH and form a high affinity for Fe^{3+} in vivo to produce iron-contained complexes with asymmetric coordination bonds that generate oxidative damages and inflammatory responses [16]. Additionally, Ferritin, as the main form of intracellular iron storage, the amino acid residues of which can directly react with CSE, to release excess free iron and furtherly cause cell death [17]. Thus, iron-involved cascades might be a critical mechanism accounting for CSE-induced BMSCs damage.

In the presence of external strong toxic stimuli, excessive input of exogenous iron or degradation of intracellular iron storage augment labial iron pool (LIP), which provokes Fenton reaction and produces large numbers of hydroxyl radicals and ROS, subsequently generates fatal concentrations of lipid hydroperoxide that destroys cellular membrane structures, and eventually results in cell ferroptosis [18]. The selective degradation of ferritin via autophagic machinery, termed as "Ferritinophagy", is critical for the regulation of cellular iron levels, characterized by Nuclear Receptor Coactivator 4 (NCOA4) serving as a selective cargo receptor for binding ferritin, forming autophagosome, and transporting to lysosomes for degradation [19]. Excessive ferritinophagy causes the occurrence and development of ferroptosis, which might act as a key mechanism of CSE-induced BMSCs death and smoking-related osteoporosis (SROP).

In the current study, we collected and compared the bone mineral density (BMD) of femoral neck in smokers and non-smokers from clinical data, and found the BMD in smokers were significantly lower than non-smokers. We constructed a rat model of SROP by intraperitoneal injection of CSE and verified CSE exposure led to a significant decrease of BMD in rats and inhibited osteogenic differentiation of rat BMSCs (rBMSCs). Transcriptomic analysis and in vitro phenotype experiments revealed that the ferroptosis pathway was significantly activated in CSE-treated rBMSCs, and AMP-activated protein kinase (AMPK) signaling was proved to be involved in the NCOA4-mediated ferritin-selective autophagy process. Furtherly, ferroptosis and ferritinophagy inhibitors significantly ameliorated BMD loss in CSE-exposed rats. Our results firstly demonstrate that rBMSCs ferroptosis is an important molecular mechanism of SROP, and provide important reference values for the prevention and treatment of osteoporosis in smokers.

2. Results

2.1. CSE exposure decreased bone mineral density in humans and rats

To verify the existence of SROP in clinical cohort, patients' data was warm-heartedly collected by our colleague Dr. Zou in Department of Orthopedics, Second Affiliated Hospital of Chongqing Medical University (*CQHS-REC-2022(LSNo.079)*). According to the Inclusion and exclusion criteria, 61 males were finally enrolled in the study with the ages between 60 and 70. Among them, 42 were smokers and the other 19 were non-smokers with no significant difference in average age (SI Fig. 1a). lower T value in the femoral neck were found in smokers which represented lower BMD (Fig. 1a-b), and were positively correlated with longer smoking years and higher accumulative smoking amount (Fig. 1c).

To further validate smoking-related bone destructions in animals, we established a rat model of SROP by intraperitoneal injection of CSE every other day for 1 month (Fig. 1d). Body weight of the CSE-exposed rats decreased significantly than that of the Control group since day 16 (SI Fig. 1b). Morphometric analysis of microcomputed tomography (micro-CT) scans exhibited significant thinner trabecular, decreased bone mass and less bone interconnection in the CSE-exposed group (Fig. 1e). Hematoxylin-eosin (H&E) staining revealed less trabecular bone and more vacuolated adipocytes in the bone marrow cavity (Fig. 1f) and Tartrate-resistant acid phosphatase (TRAP) staining presented an increasing number of osteoclasts around the epiphyseal line of femurs in the CSE-exposed rats compared to the Control group (SI Fig. 1c). Accordingly, numbers of osteoblast expressing collagen type I alpha 1 chain (Col-1) significantly diminished in the CSE-exposed rats than that of the Control group (Fig. 1f). Moreover, the terminal deoxynucleotidyl transferasemediated dUTP nick end labeling (TUNEL) assay was performed to evaluated the viability of cell around the trabecular bone, and we found a significantly enhanced number of positive staining cells was shown in the CSE-exposed group than the Control group (Fig. 1g).

To further figure out whether the differentiation capacities of bone related cells were affected by CSE exposure, we harvested rBMSCs and rat bone marrow mononuclear macrophages (rBMMs) respectively from the femurs of the CSE-exposed group and the Control group and cultured in differentiation induction medium. Not surprisingly, rBMSCs from the CSE-exposed rats showed significant fewer mineralized calcium nodules and lower expression of osteogenic differentiation marker genes (Fig. 1h), but more lipid droplets and higher expression of adipogenic differentiation marker genes (SI Fig. 1d). rBMMs from the CSE-exposed rats were more easily induced to form osteoclasts (SI Fig. 1e). In addition, CSE exposure remarkably upregulated the inflammation level of bone, as evidenced by the elevation of mRNA expression levels of IL-6, IL-1β and TNFα (SI Fig. 1f).

Collectively, we successfully established a rat model of SROP by CSE exposure, characterized by BMD decrease which is consistent with clinical data, and rBMSCs dysfunction.

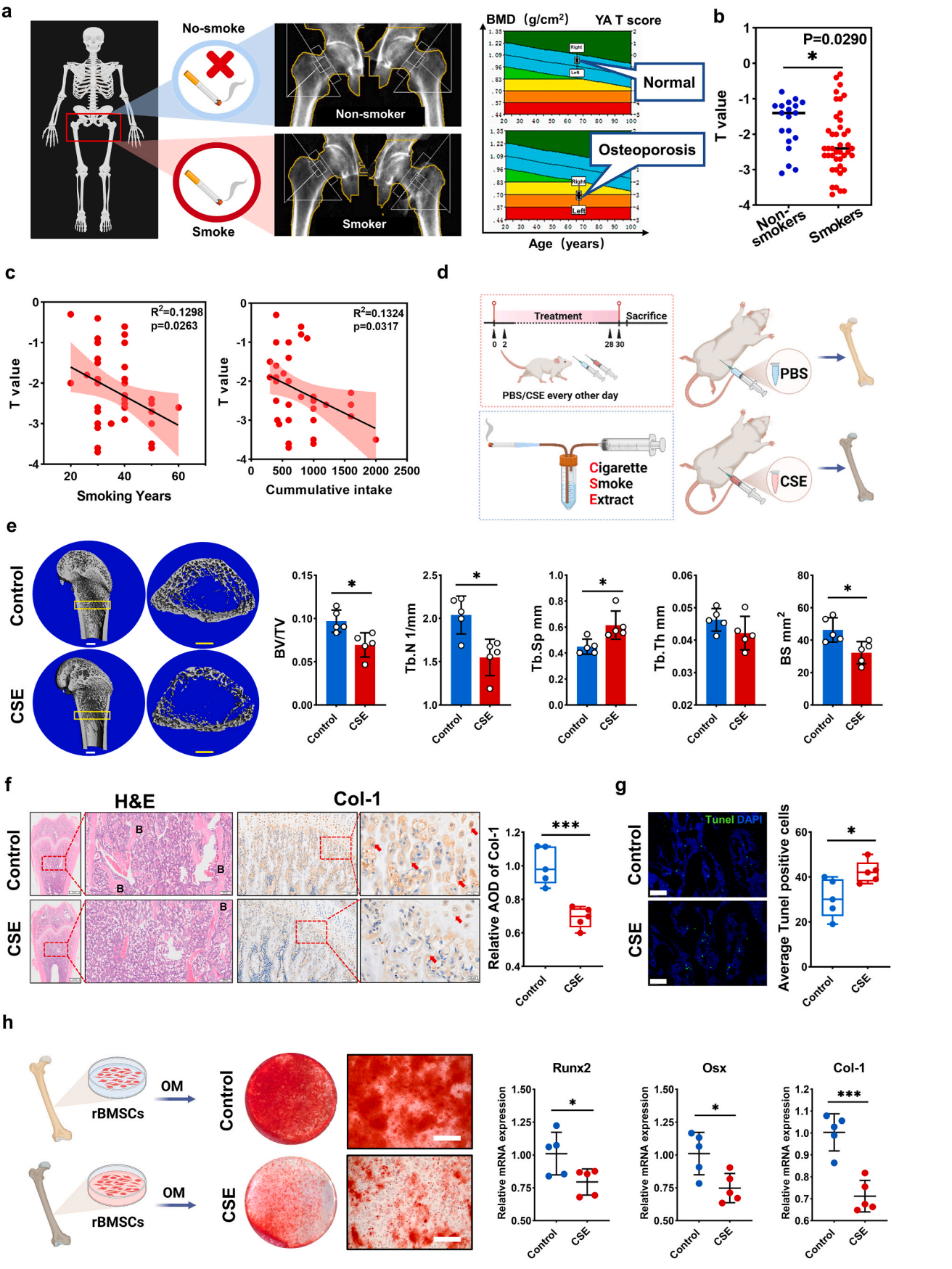

(caption on next page)

Fig. 1. CSE exposure decreased bone mineral density in humans and rats. a. Schematic diagram illustrated the representative bone mineral density (BMD) test results (radiographs and T values of femoral neck) from a non-smoker and a smoker in clinical. b. Statistical analysis of T values of non-smokers (n = 19) and smokers (n = 42). c. Statistical and correlation analysis of human BMD and cigarette smoking habits. d. Schematic diagram illustrated the operation process in the CSE-exposed and the PBS-treated rats. e. Representative reconstruction images of Micro-CT of rat distal femurs and calculations of bone morphological parameters in the regions of interest (ROI) (n = 5), scale bar:1.0 mm. f. HE staining and Col-1 IHC staining of rat distal femurs in the Control group and the CSE-exposed group, and the calculation of relative average optical density (AOD) of Col-1 (n = 5). B: bone trabecula, red arrow indicated the positive expression area for IHC staining. g. Rat femur paraffin sections subjected to TUNEL showed dead cells and statistical analysis of TUNEL positive cells (n = 5), scale bar:100 μm. h. Alizarin red staining of rBMSCs originated from rats in the Control group and the CSE-exposed group after osteogenic differentiation induction for 14 days, OM: osteogenic differentiation induction medium, scale bar: 400 μm. qPCR analysis of osteogenesis-related genes (Runx2, Osx and Col-1) of rBMSCs originated from rats in the Control group and the CSE-exposed group after osteogenic differentiation induction for 7 days (n = 5). *P < 0.05, **P < 0.01, ***P < 0.001 versus control. (For interpretation of the references to color in this figure legend, the reader is referred to the Web version of this article.)

2.2. Transcriptomic analysis and phenotype verifications revealed CSE induced ferroptosis in rBMSCs in vitro

To reveal the underlying mechanism of CSE-induced destructive effect to bone, we performed RNA-sequencing (Fig. 2a). Totally 3853 differentially expressed genes (DEGs) were identified after CSE treatment, of which 2026 genes were upregulated and 1827 genes were downregulated (Fig. 2b-c). Based on the Kyoto Encyclopedia of Genes and Genomes (KEGG) functional analysis, “Ferroptosis” pathway presented significant activated (Fig. 2d), suggesting that ferroptosis might play a very critical role involved in the damage of rBMSCs stimulated by CSE. Consistent with KEGG analysis, “iron ion homeostasis”, “cellular iron ion homeostasis”, “oxidative stress response” were also claimed as significantly upregulated biological process according to Gene Ontology (GO) analysis (Fig. 2e). Besides, we performed qPCR to verify the RNA-sequencing results (SI Fig. 2c).

To further elucidate the mechanism of ferroptosis involved in CSE-induced rBMSCs dysfunction, we performed in vitro phenotype verifications. CCK-8 results presented that CSE induced rBMSCs death in a dose- and time-dependent manner (SI Fig. 2a). Accumulation of LIP and lipid peroxidation were two typical indicators of ferroptosis. After 12h of treatment, C11-BODIPY staining showed higher ratio of FITC/Texas-red in the CSE group than in the Control group which means more obvious production of lipid peroxidation in response to CSE exposure (Fig. 2f-g). Deferoxamine (DFO), a well-known iron chelator reducing cytosolic LIP, and Ferrostatin-1 (Fer-1), a lipid ROS scavenger, are two representative inhibitors for ferroptosis. Indeed, 1h pretreatment with DFO or Fer-1 significantly attenuated CSE-induced lipid peroxidation (Fig. 2f-g) and inhibited the CSE-induced cell death and cytotoxicity evaluated by CCK-8 and LDH assay (Fig. 2h-i) in rBMSCs. However, necroptosis inhibitor necrostatin-1 (Nec-1) and apoptosis inhibitor Z-VAD-FMK showed negligible rescue effect (Fig. 2j). Subsequently, we found that 12h of CSE exposure decreased glutathione (GSH) levels of rBMSCs (Fig. 2k) and increased the cytosolic LIP based on flow cytometry of Phen Green™ SK (PGSK) signaling (Fig. 2l) and colorimetric assay (Fig. 2m). While 1h pretreatment with DFO or Fer-1 could significantly alleviate the GSH exhaustion and reduce LIP (Fig. 2k-m). Besides, we tested the protein level of solute carrier family 7 member 11 (Slc7a11) and glutathione peroxidase 4 (GPx4), two canonical repressors against ferroptosis by assisting intracellular GSH synthesis and alleviating lipid peroxidation. As expected, CSE treatment downregulated GPx4 and Slc7a11 protein levels (SI Fig. 3f), however DFO and Fer-1 could partly inhibit the reduction of GPx4 but not Slc7a11 (Fig. 2n and SI Fig. 3e). Taken together, our results indicated that CSE can induce ferroptosis in rBMSCs in vitro.

2.3. Autophagy was activated by CSE and was required for CSE-induced rBMSCs death

Accumulated evidences have uncovered the key role of autophagic machinery in driving cells toward ferroptotic death [19,20]. Consistently, the gene set enrichment analysis (GSEA) showed that the upregulated genes in the CSE-treated rBMSCs were significantly enriched in cellular components of autophagosome and secondary lysosome (Fig. 3a), thus we next investigated on the autophagic behavior of CSE-treated rBMSCs. Transmission electron microscopy (TEM) images presented more autophagosomes in CSE-treated rBMSCs (Fig. 3b). Western bolt (WB) results showed that CSE treatment time-dependently upregulated the protein ratio of LC3-II/I and decreased the expression of autophagic substrate p62, two typical markers of autophagy (Fig. 3c). Autophagy inhibitors and activators were furtherly used to verify the autophagic flux. WB analysis showed that treatment with autophagosome formation inhibitor 3-methyladenine (3-MA) and autophagy activator rapamycin (RAPA) reduced LC3-II/I ratio and p62 protein level, while blocked autophagosome degradation via chloroquine (CQ) and Bafilomycin A1 (BafA1) further increased LC3-II accumulation and p62 protein level (Fig. 3d and SI Fig. 3b). rBMSCs were transfected with adenoviral mRFP-GFP-LC3 and then treated by CSE. Most RFP-LC3 dots were calculated in the CSE group. The co-localization of mRFP-LC3 dots and GFP-LC3 dots resulted in the formation of larger yellow spots when lysosomal degradation was blocked with CQ in the CSE + CQ group according to confocal microscope images (Fig. 3e). These results demonstrated that autophagy was activated in rBMSCs stimulated by CSE. To verify autophagy dependence of CSE-induced cell death, CCK-8 assay was performed. 3-MA, BafA1 and CQ were found significantly reduce cell death by inhibiting autophagic flux at different stages, especially blocking the formation of autophagosome at early stage with 3-MA (Fig. 3f). Besides, the upregulated protein ratio of LC3-II/I and the downregulated expression of p62 were also detected in femur of the CSE-exposed rats than the Control group (Fig. 3g). Taken together, these findings indicated that CSE activated the autophagy, which was essential for the induction of cell death in rBMSCs.

2.4. Ferritinophagy was involved in CSE-induced cell death

Ferritin is the main protein for intracellular iron storage, and selective autophagic degradation of ferritin by NCOA4 has been demonstrated to accumulate labile iron and promote ferroptosis [21,22]. Herein, we focused on NCOA4-mediated ferritinophagy in CSE-treated rBMSCs. WB results revealed that Ferritin expression decreased from 0 to 12h, while NCOA4 expression increased from 0 to 1h and decreased after 1h (Fig. 4a). Inhibition of autophagy with 3-MA, BafA1 or CQ accumulated Ferritin, while induction of autophagy with RAPA upregulated the degradation of Ferritin. In CSE-exposed rBMSCs, NCOA4 expression decreased when co-cultured either with 3-MA or RAPA, but increased when co-cultured either with BafA1 or CQ (Fig. 4b and SI Fig. 4b). Immunoprecipitation analysis showed the increased binding of Ferritin with NCOA4 at 1h (Fig. 4c). Immunofluorescence analysis revealed an increased co-localization of Ferritin and LC3 in the CSE group compared to the Control group, and displayed more with additional administration of CQ in the CSE + CQ group (Fig. 4d and SI Fig. 4c). Moreover, knockdown of autophagy related 5 (ATG5, a key protein forming complex which is necessary for LC3-I transforming to LC3-II) and NCOA4 by siRNA significantly reduced the degradation of Ferritin along with alleviating cell death and lipid peroxidation damage (Fig. 4e–h).

Besides, we tested ferroptosis signals in vivo. As expected, CSE upregulated the expression of two lipid peroxidation biomarkers,

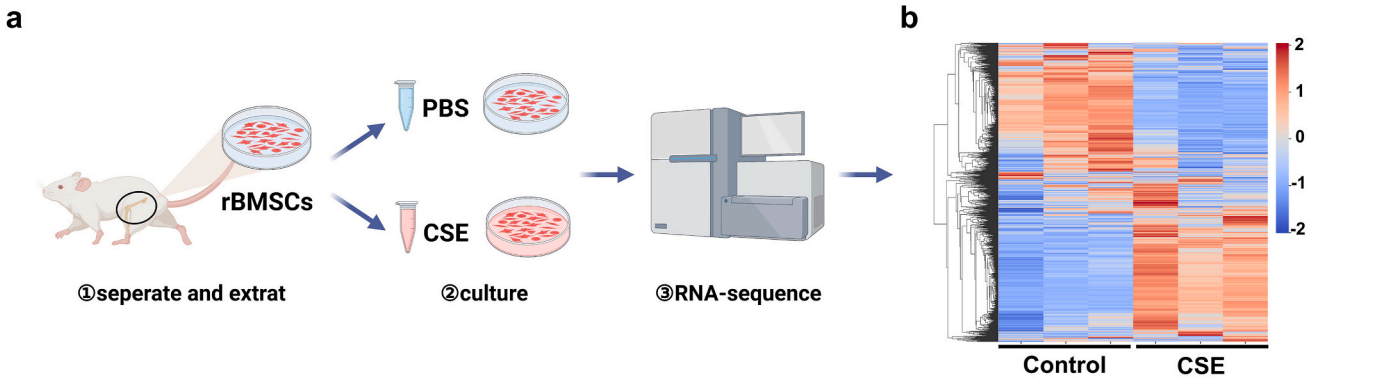

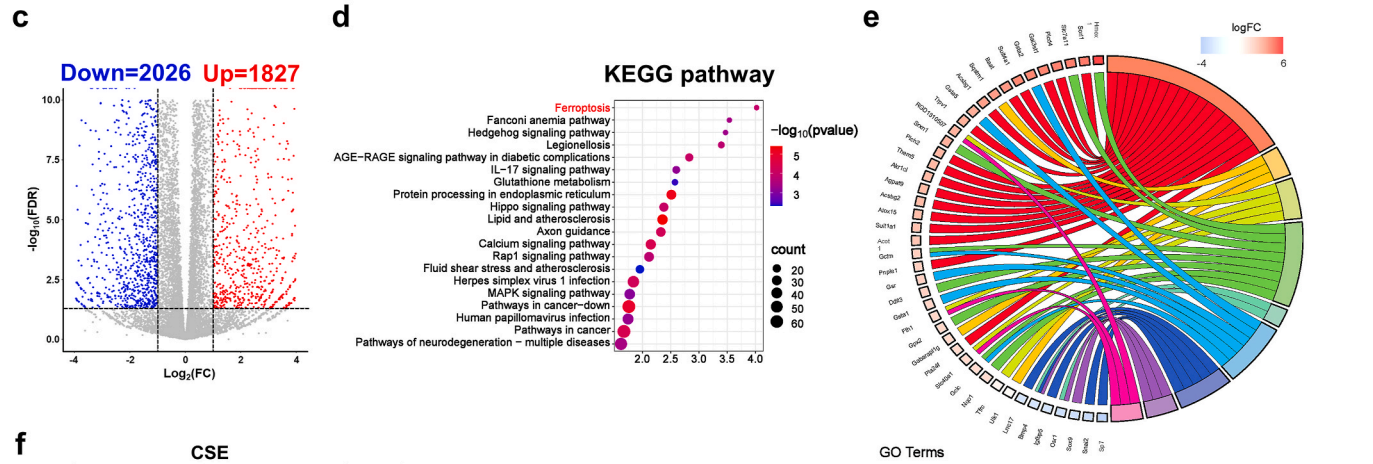

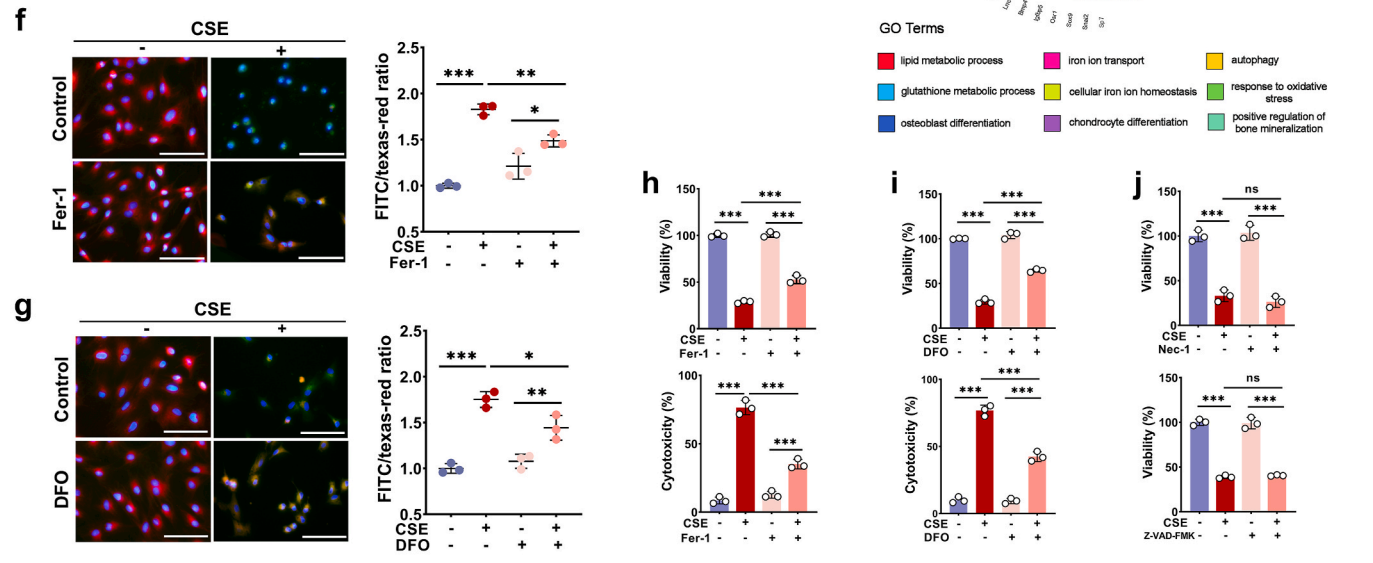

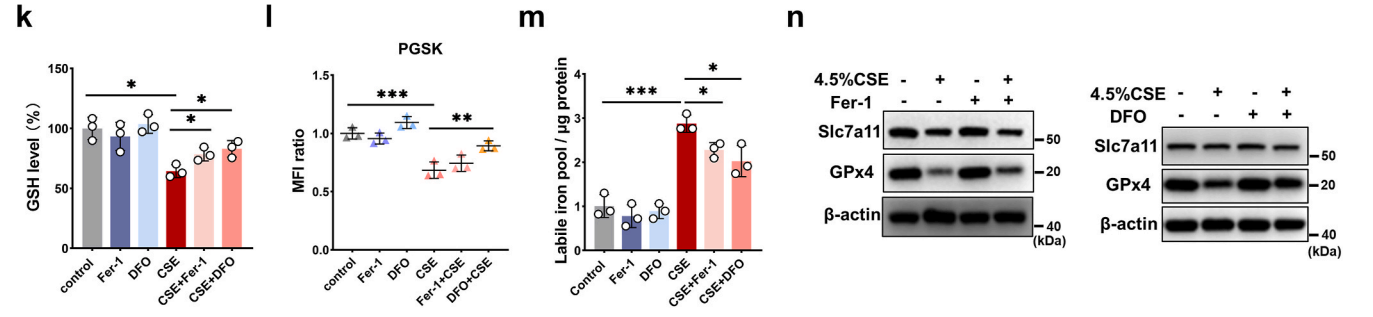

(caption on next page)

Fig. 2. Transcriptomic analysis and phenotype verifications revealed CSE induced ferroptosis in rBMSCs in vitro. a. Schematic illustration of the experimental design and sample preparation for transcriptomic analysis. b. Heatmap showed differentially expressed genes (DEGs) between rBMSCs from the Control and the CSE group (n = 3 in each group). Red: up-regulated expression levels. Blue: down-regulated expression levels. c. Volcano map showed the DEGs. d. KEGG analysis of the DEGs was carried out, and Top 20 of the pathways with significant enrichment were shown. e. GO Chord plot according to GO enrichment analysis displayed the relationship between the significant upregulated terms and genes, including "lipid metabolic process", "glutathione metabolic", "iron ion transport", "cellular iron ion homeostasis", "response to oxidative stress", "autophagy", and downregulated terms including "osteoblast differentiation", "chondrocyte differentiation", "positive regulation of bone mineralization". f-g. Representative microscopy images and calculation of FITC/texas-red ratio of lipid peroxidation assay in rBMSCs following PBS or 4.5 % CSE treatment for 12h combined with Fer-1 (2 μM) or DFO (1 μM) (n = 3), scale bar:100 μm. h-j. Cell viability was assessed by CCK-8 assay and cell death was evaluated by cytotoxicity using LDH assay of rBMSCs with PBS or 4.5 % CSE treatment for 12h combined with Fer-1 (2 μM), DFO (1 μM), Nec-1 (10 μM) or Z-VAD-FMK (20 μM). Relative GSH levels of rBMSCs (k), Mean fluorescence intensity (MFI) analysis of PGSK-labeled rBMSCs (l), LIP concentration of rBMSCs (m), WB showing expression level of Slc7a11 and GPx4 of rBMSCs (n) with PBS or 4.5 % CSE treatment for 12h combined with Fer-1 (2 μM) or DFO (1 μM) (n = 3). *P < 0.05, **P < 0.01, ***P < 0.001 versus control. (For interpretation of the references to color in this figure legend, the reader is referred to the Web version of this article.)

malondialdehyde (MDA) (SI Fig. 3f) and 4-hydroxynonenal (4-HNE) (SI Fig. 3d). The upregulated mRNA expression level of Prostaglandin-endoperoxide synthase 2 (PTGS2) and the downregulated mRNA expression level of Ferritin, NCOA4 and GPx4 (SI Fig. 3e) as well as the downregulated protein level of Ferritin (SI Fig. 3g) revealed that CSE also disrupted iron homeostasis and activated ferroptosis signals in vivo.

Collectively, these observations highly suggested NCOA4-mediated autophagic-dependent ferroptosis might be the key mechanism involved in the damage process of CSE both in vitro and in vivo.

2.5. ROS and mitochondrial damage activated AMPK and furtherly promoted CSE-induced ferritinophagy in rBMSCs

To further explore the regulator of ferritinophagy activation in response to CSE, we noticed that mammalian target of rapamycin (mTOR) signaling pathway was significantly down regulated and Adenosine monophosphate (AMP) metabolic process was significantly activated according to GSEA analysis (Fig. 5a and SI Fig. 5a). AMPK and mTOR, as key sensors of oxidation-reduction and energy status in cells, regulate the autophagic turnover through mediating unc-51 like autophagy activating kinase 1 (ULK1) [23]. It is claimed that the feedback loops of the AMPK/mTOR/ULK1 regulatory triangle guarantee the appropriate response mechanism when triggered by diverse stimuli [24]. Since we detected the most obvious combination of Ferritin and NCOA4 was at 1h, we firstly evaluated the activity of AMPK/mTOR/-ULK1 from 0 to 60min. WB results presented that CSE exposure induced elevation of p-AMPK (Thr172) and p-ULK1 (Ser555), and reduction of p-mTOR (Ser2448) (Fig. 5b and SI Fig. 5b), along with rapid activation of autophagy and ferritinophagy (Fig. 5c and SI Fig. 5d). Importantly, the expression of Transferrin receptor (TFRC) was observed to increase from 0 to 60 min, indicating that the iron entry channels on rBMSCs were activated promptly upon CSE stimulation. Consequently, iron, being one of the components of CSE, entered into the rBMSCs and contributed to the development of iron-related cytotoxicity (Fig. 5d and SI Fig. 5e). 2,7-dichlorofluorescein diacetate (DCFH-DA) staining confirmed rapid enhancement of ROS at 1h (Fig. 5e). According to the CCK-8 result in Fig. 3f, mTOR-dependent autophagy inducers RAPA had scarce influences on the rBMSCs death induced by CSE, we speculated that mTOR signaling might not be a major contributor. While AMPK knockdown significantly reversed the degradation of Ferritin and protein ratio of LC3-II/I (Fig. 5f and SI Fig. 5f), rescued cell death and alleviated lipid peroxidation (Fig. 5g) induced by CSE. The similar rescue effect was also found in AMPK inhibitor Compound C-treatment group with CSE (SI Fig. 5g). Our results demonstrated that AMPK/ULK1 is associated with CSE-induced ferritinophagy activation.

Subsequently, we further explored the AMPK/ULK1 at later time point after 1h. The protein level of p-AMPK (Thr172) and p-ULK1 (Ser555) exhibited a fluctuated variation, which down-regulated after 1h, reached the lowest expression level at 3h and then elevated till the end time point (Fig. 5h and SI Fig. 6a). AMPK is recognized as a key sensor reflecting the function and states of mitochondria, while mitochondria are the nexus of stress actively involved in different types of regulated cell death mechanisms [25]. Since the essential role of mitochondria in regulating the initiation and progress of ferroptotic death in cells is still controversial [26,27], we next attempt to elucidate the contribution made by mitochondria in the process of CSE-induced rBMSCs ferroptosis. TEM observations revealed that CSE treatment caused swollen mitochondria characterized by severely disrupted cristae (Fig. 5i). Fluorescence staining and flow cytometry revealed that CSE exposure increased mitochondrial ROS (mROS) production in rBMSCs (Fig. 5j and SI Fig. 6c). Mitochondrial membrane potential (MMP) and Adenosine Triphosphate (ATP) production was detected significantly elevated at 3h and eventually collapsed at 12h (Fig. 5k&5l). These results were unlike with hydrogen peroxide (H_2O_2)-induced cell injury through devastating MMP and decreasing ATP synthesis, but more like ferroptotic cell death characteristics [28]. The collapse of MMP reactivated AMPK signals at second stage from 3 to 12h and promoted ferritinophagy-regulated rBMSCs ferroptosis. N-acetyl-L-cysteine (NAC) as an intracellular ROS scavenger, Mitoquinone mesylate (MitoQ) as a mitochondrion-targeted ROS scavenger, were both found to significantly rescue cell viability (Fig. 5m) and decrease lipid peroxidation (Fig. 5n) upon CSE exposure. NAC were furtherly observed to restore MMP (Fig. 5o), down-regulate the expression of p-AMPK/AMPK, p-ULK1/ULK1 and LC3-II/I, and up-regulate that of , Ferritin, p62, Slc7a11 and GPx4 in rBMSCs (Fig. 5p and SI Fig. 6d).

Taken together, exogenous ROS and iron in CSE firstly induce AMPK-regulated autophagic dependent Fenton reaction, which furtherly attacked mitochondria boost endogenous ROS and aggravated rBMSCs ferroptosis.

2.6. Ferritinophagy and ferroptosis inhibition ameliorated SROP in rats

We conducted further investigations to explored the therapeutic impact of ferritinophagy and ferroptosis inhibitors on the damaged bone induced by CSE in rats (Fig. 6a). Ferritinophagy inhibitor 3-MA and ferroptosis inhibitors DFO and Fer-1 pretreated 7days significantly alleviated the decrease of BMD according to calculated indicators (Fig. 6b-c), reduced the expression of oxidative stress production by IHC staining of 4-HNE (Fig. 6d) and MDA content assay (Fig. 6e), increased the Col-1 expression (SI Fig. 7d) and reduced the osteoclast numbers (SI Fig. 7e) compared to the CSE-exposed group. Moreover, inflammation indicators IL-6, IL-1β and TNFα (SI Fig. 7c) and ferroptosis-related indicators PTGS2 (Fig. 6f) were downregulated, and Ferritin, NCOA4 and GPx4 (Fig. 6f) were upregulated in the 3-MA, DFO, and Fer-1 treated rat femur in gene expression. WB results further disclosed that the protein level of Ferritin and NCOA4 were restored in 3-MA, DFO, and Fer-1 treatment groups in vivo (Fig. 6g). Collectively, our results indicated that inhibition of ferritinophagy and ferroptosis signaling is a feasible strategy for reversing bone damage in the CSE-exposed rats.

3. Discussion

In the present study, the clinical data were collected to compared the BMD values of femoral neck between smokers and non-smokers. The

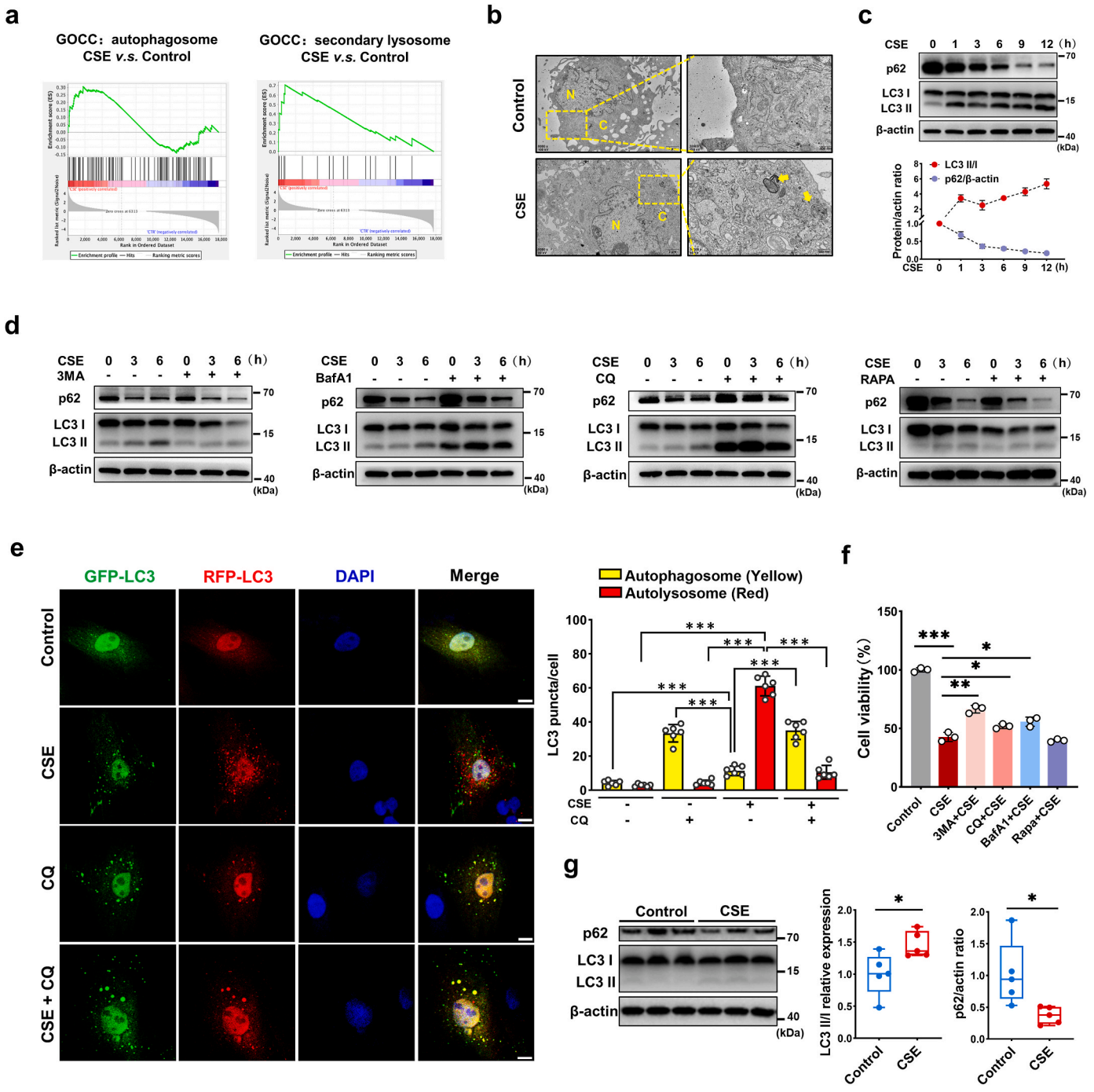

Fig. 3. Autophagy was activated by CSE and was required for CSE-induced rBMSCs death. a. GSEA analysis showed significant difference in "autophagosome" and "secondary lysosomes" by GOCC enrichment in the CSE-treated rBMSCs compared to the Control group. b. Representative TEM images of autophagic vacuole in rBMSCs following 4.5 % CSE treatment for 3h. Yellow arrows indicated autophagic vacuole. c. WB showing expression level of LC3-II/I and p62 in rBMSCs treated with 4.5 % CSE for 0,1,3,6,9,12h (n = 3). d. WB showing expression level of LC3-II/I and p62 in rBMSCs following 4.5 % CSE treatment for 3h and 6h combined with 3-MA (20 μM), BafA1(100 nM), CQ (10 μM) and RAPA (50 nM). E. Fluorescence confocal images of mRFP-GFP-LC3 adenovirus-transfected rBMSCs treated with 4.5 % CSE. Red signal indicated autophagolysosome, green signal indicated autophagosome, and yellow signal indicated red and green superposition. Scale bar = 10 μm. Statistical graph of LC3 puncta per cell were calculated in indicated groups, n = 6. f. CCK-8 assay of rBMSCs treated with 4.5 % CSE for 6h combined with 3-MA (20 μM), BafA1(100 nM), CQ (10 μM) and RAPA (50 nM) (n = 3). g. WB showing expression level of LC3-II/I and p62 of rat distal femurs in the Control group and the CSE-exposed group (n = 5). *P < 0.05, **P < 0.01, ***P < 0.001 versus control. (For interpretation of the references to color in this figure legend, the reader is referred to the Web version of this article.)

results presented that the smokers had significantly lower BMD values. In addition, BMD loss and inferior osteogenic differentiation of rBMSCs were also detected in the CSE-exposed rat model. RNA-sequence revealed that the biological process of ferroptosis was significantly activated. Subsequent phenotype experiments demonstrated CSE induced ferroptosis in rBMSCs along with LIP accumulation and lipid peroxidation, and this cell death process was dependent on NCOA4-mediated ferritinophagy. Further verifications indicated ROS and mitochondrial damage activated AMPK and might be the upstream regulator of CSE-induced ferritinophagy. Notably, ferritinophagy

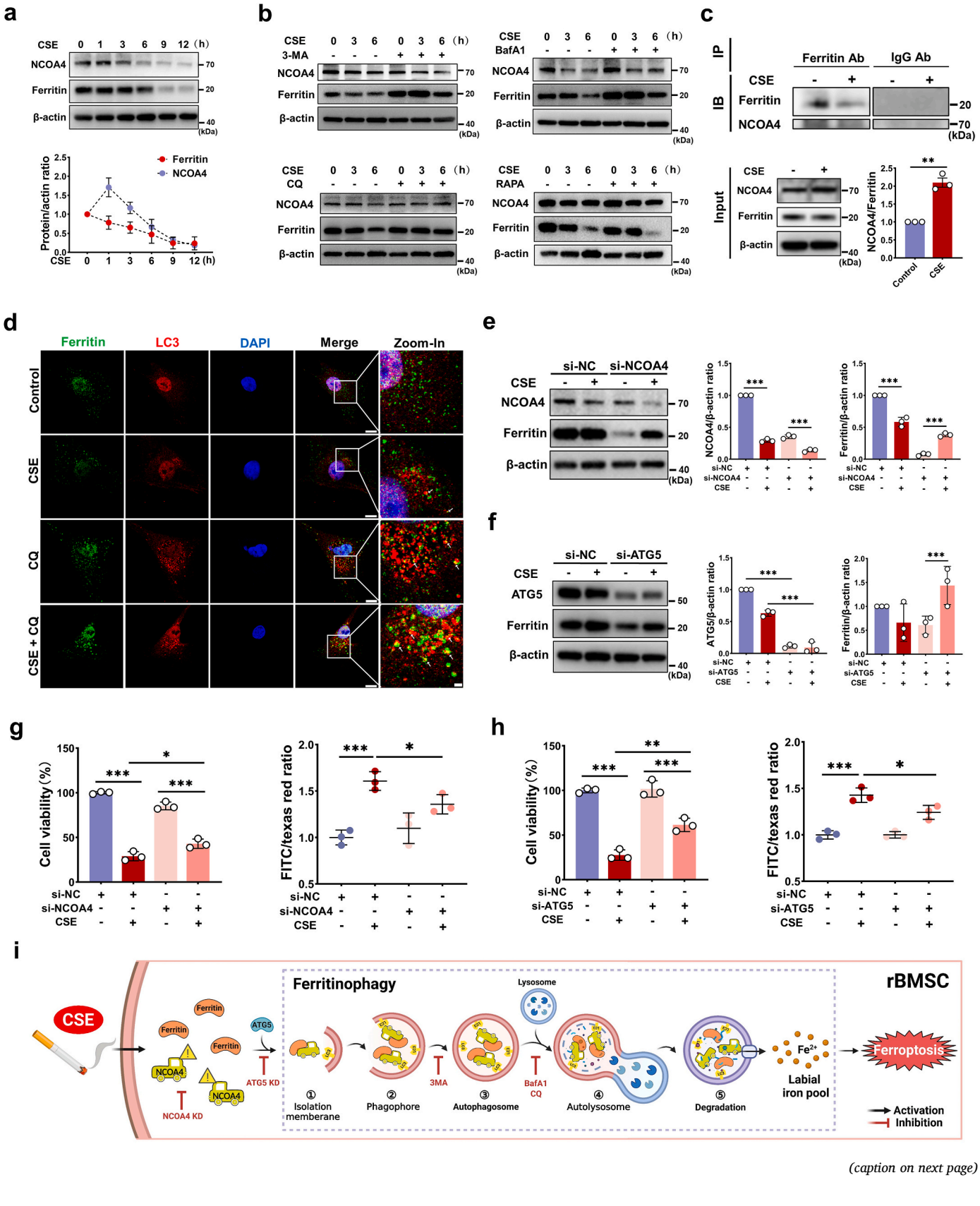

(caption on next page)

Fig. 4. Ferritinophagy was involved in CSE-induced cell death. a. WB showing expression level of Ferritin and NCOA4 in rBMSCs treated with 4.5 % CSE for 0,1,3,6,9,12h (n = 3). b. WB showing expression level of Ferritin and NCOA4 in rBMSCs following 4.5 % CSE treatment for 3h and 6h combined with 3-MA (20 μM), BafA1(100 nM), CQ (10 μM) and RAPA (50 nM). c. Co-immunoprecipitation of Ferritin-NCOA4 formation in rBMSCs treated with 4.5 % CSE for 1h (n = 3). d. Immunofluorescence colocalization of Ferritin and LC3 in rBMSCs treated with 4.5 % CSE for 6 h combined with CQ (10 μM). Green signal indicated Ferritin, red signal indicated LC3, Nuclei were counterstained with DAPI (blue signal), yellow signal indicated colocalization region of green and red, scale bar:25 μm. e. WB showing expression level of Ferritin and NCOA4 in rBMSCs after 4.5 % CSE treatment for 12h following NCOA4 knockdown (n = 3). f. WB showing expression level of Ferritin and ATG5 in rBMSCs after 4.5 % CSE treatment for 12h following ATG5 knockdown (n = 3). g. CCK-8 assay and C11-BODIPY 581/591 analysis of rBMSCs after 4.5 % CSE treatment for 12h following NCOA4 knockdown (n = 3). h. CCK-8 assay and C11-BODIPY 581/591 analysis of rBMSCs after 4.5 % CSE treatment for 12h following ATG5 knockdown. i. Schematic diagram illustrated the activated process of Ferritinophagy in rBMSCs treated with CSE, which was blocked by NCOA4/ATG5 knockdown and autophagy inhibitors. *P < 0.05, **P < 0.01, ***P < 0.001 versus control. (For interpretation of the references to color in this figure legend, the reader is referred to the Web version of this article.)

inhibitor 3-MA and ferroptosis inhibitors DFO and Fer-1, significantly ameliorated smoking-related BMD loss and restored redox balance in the CSE-exposed rats. Taken together, these findings established a novel role of rBMSCs ferroptosis in the pathogenesis of SROP.

Latest studies support that ferroptosis might be a new therapeutic target for the treatment of osteoporosis. High blood glucose, long-term use of high-dose steroid hormones, and estrogen deficiency have been reported to elicit iron homeostasis imbalance and ultimate led to the development of osteoporosis [29]. Herein, our RNA-sequence results revealed significant alterations in the expression of genes related to "cellular iron homeostasis" and "ferroptosis" in CSE-treated rBMSCs, strongly suggested ferroptosis might play a crucial role in the pathogenesis of SROP. System Xc-/GSH/GPx4 axis is currently the most studied anti-ferroptosis mechanism [30]. In our study, CSE treatment downregulated GPx4 and Slc7a11 protein levels, while Fer-1 and DFO alleviated cell death with partially recovering the expression of GPx4 but not Slc7a11. We speculated that CSE might not only deplete the intracellular antioxidants but also attack System Xc- channels and imped amino acid exchange, similarly to Erastin (a typical ferroptosis inducer) which had been previously reported [31]. Though CSE as a complex mixture contains complicated biological effects and is hardly ascribed to one specific cell cytotoxicity, in the present study we clearly demonstrated that CSE-induced rBMSCs death is at least partially attributable to ferroptosis.

Increasing evidences elucidated the role of autophagy in driving cells towards ferroptotic death [19,32,33]. Besides, latest Transcriptome-Wide Association Study reported that cigarette smoking among common lifestyles showed the strongest correlation with human BMD, and microtubule-associated protein 1 light chain 3B (MAP1LC3B) was a candidate gene significantly associated with both BMD and cigarette smoking [34]. We next explored the correlation and causality between autophagy and CSE-induced rBMSCs ferroptosis. Our results validated that CSE activated autophagy in rBMSCs and demonstrated ferritinophagy was required for rBMSCs ferroptosis. While ferritinophagy has been involved in various pathological processes, not all the researchers have reported consistent results regarding the expression of NCOA4 during ferritinophagy [18,19,32]. Based on our findings on the expression of NCOA4 and TFRC, as well as the results of Co-IP analysis from 0 to 1h, we hypothesized that during the early stage, Fenton reaction occurred rapidly due to an increase in LIP which was caused by direct iron influx from CSE and indirectly autophagic degradation of Ferritin stimulated by abundance of oxidants from CSE. As the cytoplasmic LIP levels continued to rise, NCOA4 might gradually degrade for the following two pathways: 1) through excessive autophagy along with Ferritin in autolysosome [32] or 2) through the ubiquitin-proteasome pathway after being ubiquitinated [35]. Importantly, we verified NCOA4 knockdown significantly reduced lipid peroxidation, cytosolic LIP and Ferritin degradation, and rescued rBMSCs death. These results indicated that excessive ferritinophagy, mediated by NCOA4, disrupted iron homeostasis and promoted ferroptosis in rBMSCs exposed to CSE.

Autophagy modulators (e.g., BECN1, STING1/TMEM173, CTSB, HMGB1, PEBP1, MTOR, AMPK, and DUSP1) were reported to determine the ferroptotic response in a context-dependent manner [36], we thus conducted additional researches to investigate the potential mechanisms regulating ferritinophagy. Latest investigation demonstrated AMPKα activation by accumulation of tobacco toxins in body was critical and therefore accelerated the progression of non-alcoholic fatty liver disease (NAFLD) [37]. In the present study, the phosphorylation of AMPK at Thr172 occurred in two separate sessions at 0–1h and 3–12h. Correspondingly, an increase in MMP and ATP synthesis was observed at 3h, followed by a decline at 12h, and this was not entirely consistent with previous studies on tobacco toxicity [38], but more in line with the reported mitochondrial characteristics in ferroptosis [28]. We suggest CSE-induced rBMSCs ferroptosis might be divided into 2 stages. In the initial stage from 0 to 1h, AMPK was rapidly activated by oxidants from CSE, leading to an increase in LIP and subsequently initiation of the Fenton reaction, resulting in the destruction of phospholipid structure including mitochondria. Previous research indicated that cysteine deprivation promoted the tricarboxylic acid (TCA) cycle and enhanced electron chain transfer, leading to hyperpolarization of MMP and accumulation of lipid peroxide, and ultimately culminating in cell ferroptosis [39]. In our study, the downregulation of Slc7a11 suggested the amino acid exchange of System Xc- was damaged by CSE thereby blocking the entry of cysteine into the cell, and this led to the consumption of intracellular GSH and subsequent hyperpolarization of the mitochondria. In the later stage from 3 to 12h, the mitochondria were continually subjected to the attacked by ROS generated from Fenton reaction and the MMP was thus collapsed which furtherly produce endogenous ROS activated AMPK signaling. Notably, the total protein and phosphorylation levels of AMPK were downregulated from 1 to 3h. Previous studies have also reported that AMPK inactivation promoted ferroptosis through a non-autophagic pathway by failing to inactivate acetyl-CoA carboxylase thus accumulating excess lipid peroxidation [40]. In our study, we observed that AMPK knockdown and AMPK inhibitor Compound C significantly rescued cell viability and lipid peroxidation of rBMSCs exposed to CSE, we suggested AMPK-mediated non-autophagic mechanism might be involved in the CSE-induced rBMSCs ferroptosis at some extent, but not the main reason. Collectively, our data supported AMPK activation by ROS and mitochondrial damage served as the upstream regulator of CSE-induced ferritinophagy and ferroptosis in rBMSCs.

For further elucidate the crucial role of ROS originating from CSE and mitochondrial damage in rBMSCs ferroptosis, MitoQ and NAC were used in the following experiments. As expected, MitoQ and NAC significantly restored the viability and reduced the lipid peroxidation of rBMSCs, with NAC exhibiting a more pronounced effect. NAC extensively cleared the intracellular ROS and acted as a precursor replenishment for GSH synthesis, and thereby reduced the lipid peroxide levels, which supported our hypothesis regarding the "two stages of CSE-induced rBMSCs ferroptosis", wherein exogenous ROS from CSE initially triggered AMPK-regulated autophagic dependent Fenton reaction, which attacked mitochondria furtherly boost endogenous ROS and aggravated ferroptotic death in rBMSCs.

One of the particular challenges in our study is to develop a SROP animal model. Previous studies chose nicotine, known as the main contributor of cigarette toxicity, through intraperitoneal injections or subcutaneous implant [41]. However, cigarette smoke composes over 7000 chemicals with multiple influence [15], and is difficult to be

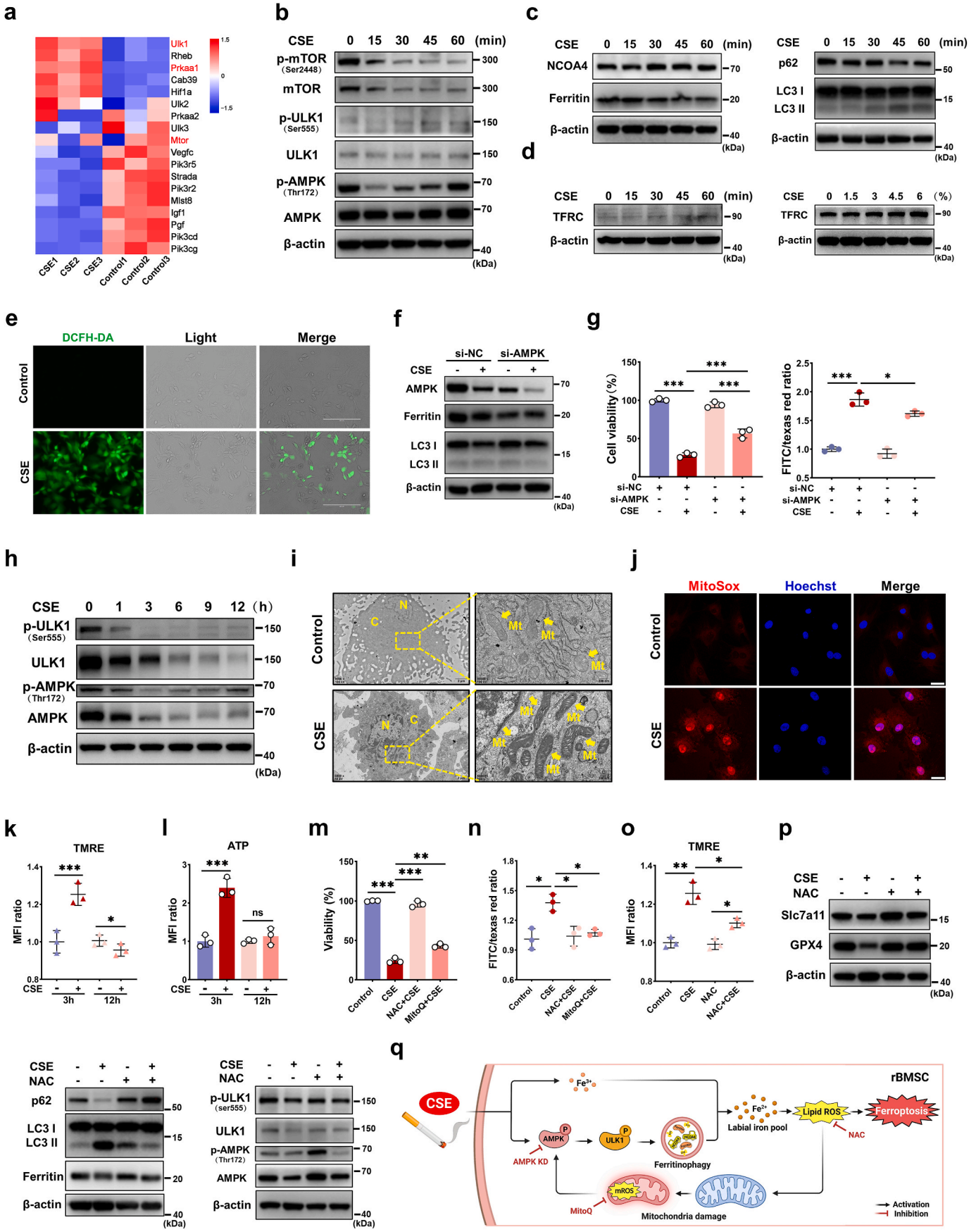

(caption on next page)

Fig. 5. ROS and mitochondrial damage activated AMPK and furtherly promoted CSE-induced ferritinophagy in rBMSCs a. GSEA analysis presented gene expression in mTOR signaling pathway. b. WB showing expression level of p-mTOR, mTOR, p-ULK1, ULK1, p-AMPK and AMPK in rBMSCs treated with 4.5 % CSE for 0, 15, 30, 45 and 60 min. c. WB showing expression level of Ferritin, NCOA4, LC3-II/I and p62 in rBMSCs treated with 4.5 % CSE for 0,15,30,45 and 60 min. d. WB showing expression level of TFRC in rBMSCs treated with 4.5 % CSE for 0,15,30,45 and 60 min and with 0,1.5,3,4.5,6 % CSE for 1h. e. Representative microscopy images of DCFH-DA staining in rBMSCs treated with 4.5 % CSE for 1h, scale bar: 100 μm. f. WB showing expression level of AMPK, Ferritin and LC3-II/I in rBMSCs after 4.5 % CSE treatment for 12h following AMPK knockdown. g. CCK-8 assay and C11-BODIPY 581/591 analysis of rBMSCs after 4.5 % CSE treatment for 12h following AMPK knockdown. h. WB showing expression level of p-ULK1, ULK1, p-AMPK and AMPK in rBMSCs treated with 4.5 % CSE for 0,1,3,6,9,12h. i. Representative TEM images of mitochondria in rBMSC treated with 4.5 % CSE for 3h. Yellow arrows showed swollen mitochondria with severely disrupted cristae. j. Representative fluorescence confocal images of mROS with MitoSox dye in rBMSCs treated with 4.5 % CSE for 3h. Scale bar = 25 μm. k. Flow cytometry of mitochondrial membrane potential labeled by TMRE in rBMSCs treated with 4.5 % CSE for 3h and 12h (n = 3). l. ATP production detection of rBMSCs following 4.5 % CSE treatment for 3h and 12h (n = 3). m. CCK-8 assay (m) and C11-BODIPY 581/591 analysis (n) of rBMSCs treated with 4.5 % CSE for 12h combined with NAC (2 mM) or MitoQ (5 μM) (n = 3). o. Statistical analysis of mean fluorescence intensity (MFI) of TMRE-labeled rBMSCs following 4.5 % CSE treatment for 12h combined with NAC (2 mM) (n = 3) p. WB showing expression level of Slc7a11, GPx4, p62, LC3-II/I, Ferritin, p-AMPK, AMPK, p-ULK1 and ULK1 in rBMSCs treated with 4.5 % CSE combined with NAC (2 mM). q. Schematic diagram illustrated exogenous ROS and iron in CSE firstly induce AMPK-regulated autophagic dependent Fenton reaction, which attacked mitochondria furtherly boost endogenous ROS and aggravated ferroptotic death. *P < 0.05, **P < 0.01, ***P < 0.001 versus control. (For interpretation of the references to color in this figure legend, the reader is referred to the Web version of this article.)

representative by nicotine. Thus, we opted a CSE model. Besides, it is worth to note that smoke fumigation is a more commonly used exposure model by passive inhalation of cigarette smoke directly from respiratory tract. While this method has several shortcomings for bone-related studies, including indirect influence, time-consuming and difficulty in controlling the exposure dosage. CSE exposure to cells and model animals had been previously proved to be an efficacious method for studying on bone remodeling [42]. Our in vivo data showed that a SROP rat model by CSE exposure was successfully established and also revealed the crucial role of inhibiting ferritinophagy and ferroptosis in ameliorating bone destruction of rats exposed to CSE.

There are still limitations exist in our studies. Osteoporosis is a metabolic bone disease that occurs due to an imbalance that osteoblastic bone formation fails to compensate osteoclastic bone resorption. In this study we mainly focused on CSE-induced ferroptosis in BMSCs, while the major cells directly responsible for bone formation are osteoblasts. Previous researches had reported that CSE affected the viability and osteogenic differentiation potential of osteoblasts by causing oxidative stress damage [43,44]. But the relevant mechanism is still not yet fully explained. On the one hand, recent findings have reported the causal role of ferroptosis cascade in cigarette smoke-mediated toxicity and cell death, and thus CSE-activated ferroptosis pathway might not be a unique occurrence. On the other hand, osteoblasts are derived from BMSCs and osteoblastic bone formation is mediated by BMSCs, and CSE-induced ferroptosis can also be observed in primary osteoblasts (SI Fig. 8). This further emphasizes the critical role of ferroptosis in the pathogenesis of SROP. In addition, we observed enhanced osteoclast differentiation of rBMMs from CSE-exposed rats (SI Fig. 1e) and augmented osteoclast numbers in femur (SI Fig. 1c), suggesting the increased osteoclastic bone resorption is also an important aspect should not be ignored in the pathogenesis of SROP. Therefore, more investigations should be designed for further elucidation. Besides, further in vivo evidence such as rBMSCs specific NCOA4 knockout mice is needed to support the role of NCOA4 in the development of SROP.

In summary, our findings supported the notion that an imbalance in iron homeostasis regulated by ferritinophagy in rBMSCs, played a critical role in the pathogenesis of SROP. Accumulation of ROS and LIP led to lipid peroxidation which subsequently triggered ferroptosis in rBMSCs and this process was proved to be mediated by AMPK and dependent on NCOA4-regulated ferritinophagy. Furthermore, the administration of 3-MA, DFO, and Fer-1 were found to ameliorate trabecular deterioration in the CSE-exposed rats respectively. We believe that our study provides important clues into the rBMSCs cytotoxicity induced by CSE, developed a novel insight for SROP pathogenesis targeting ferroptosis, and suggested potential values for prevention and treatment of osteoporosis in smokers.

4. Materials and methods

4.1. Materials and reagents

Ferrostatin-1 (Fer-1, HY-100579), Necrostatin-1(Nec-1, HY-15760), Z-VAD-FMK (HY-16658B), 3-methyladenine (3-MA; HY-19312), Mitoquinone mesylate (MitoQ, HY-100116A), were obtained from MedChemExpress (MCE, USA). Chloroquine diphosphate salt (CQ, C6628), Bafilomycin A1 (BafA1, B1793), Rapamycin (RAPA, V900930), N-acetyl-L-cysteine (NAC, A9165), Deferoxamine mesylate salt (DFO, D9533), were obtained from Sigma-Aldrich (St. Louis, MO, USA). BODIPY™ 581/591C11 (Lipid Peroxidation Sensor, D3861), iron florescent probe Phen Green™ SK (PGSK, P14313) and mitochondrial ROS probe MitoSox (M36008) were obtained from Thermo Fisher Scientific (USA). Hoechst33342 (C1022), Tetramethylrhodamine ethyl ester perchlorate (TMRE, C2001S) and 2,7-dichlorofluorescein diacetate assay kit (DCFH-DA, S0033S), were purchased from Beyotime (Beijing, China).

4.2. Cigarette smoke extract (CSE) preparation

Cigarette smoke extract (CSE) was prepared as previously reported with minor modifications [45]. For in vitro study, about 50 ml of cigarette smoke were drawn into syringe and bubbled into sterile phosphate buffered saline (PBS) in 15-ml BD falcon tubes, with 2-s puff duration and 60-s puff interval. We used one cigarette (Marlboro) for 10 ml of PBS. To ensure a similar preparation amongst different batches, CSE concentration was determined spectrophotometrically at 320 nm wavelength in a plate reader (BMG Labtech GmbH, Offenburg, Germany) [46]. This solution was considered to be 100 % CSE, filtered through a 0.22 μm-pore filter and immediately aliquoted and kept at −80 °C avoiding of repeated freezing and thawing. For in vivo study, we used one cigarette for 1 ml of sterile PBS and immediately intraperitoneal injected rats after being filtered through a 0.22 μm-pore filter.

4.3. Human samples

Human data were collected from hospitalized male patients between 60 and 70 years of age from 2016 to 2019 in Department of Orthopedics, Second Affiliated Hospital of Chongqing Medical University. We recorded the T value from BMD test and smoking habits from the medical reports. Patients with systematic disease such as diabetes, malignant cancer were excluded. They were informed with our objective of investigation and agreed to offer relevant data. The human study of this research was conducted in accordance with The Code of Ethics of the World Medical Association (Declaration of Helsinki) and was approved by the Ethical Committee of the affiliated Hospital of Stomatology of Chongqing Medical University (*approval number: CQHS-REC-2022 (LSNo.079)*). The privacy rights of human subjects were always be

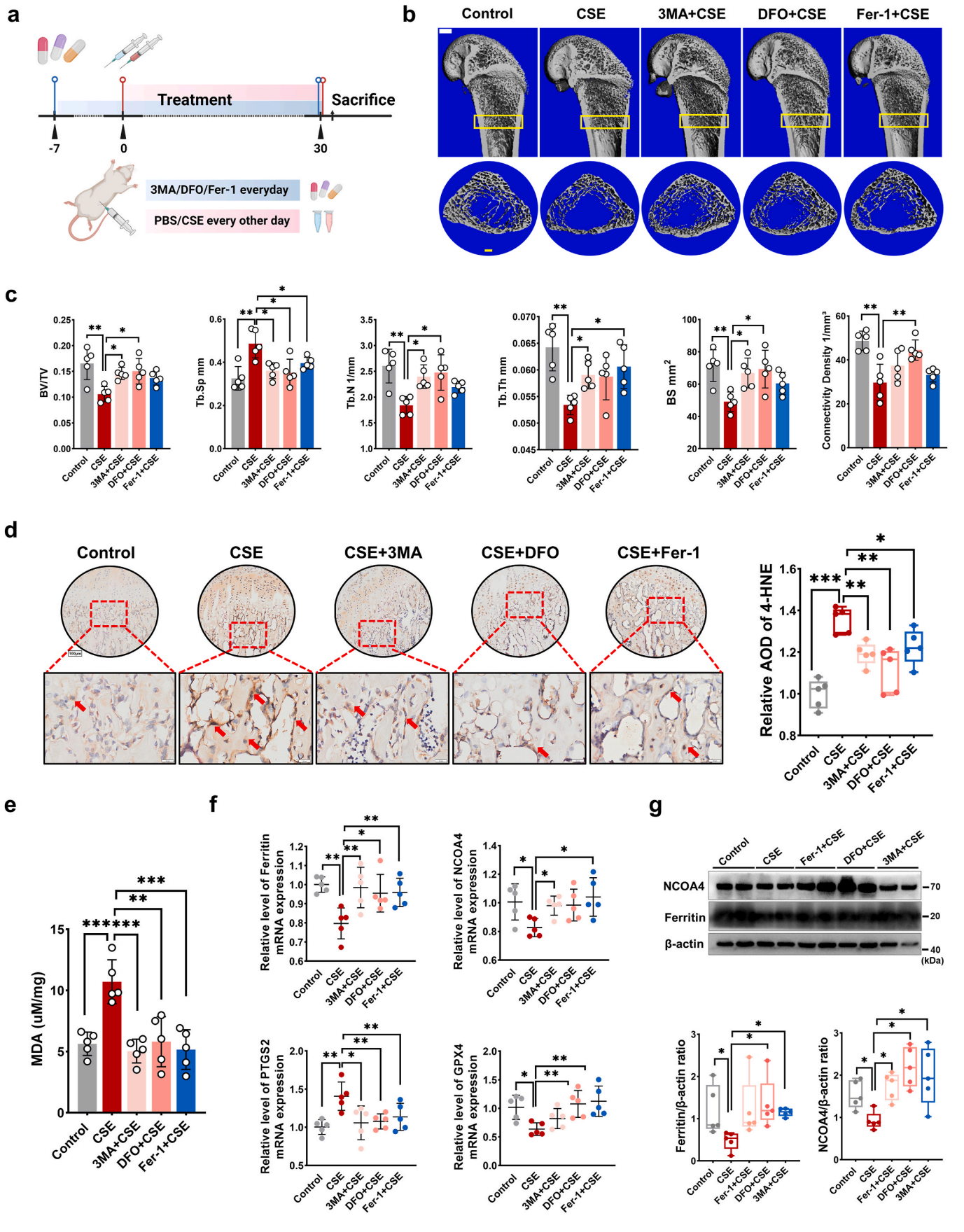

(caption on next page)

Fig. 6. Ferritinophagy and ferroptosis inhibition ameliorated SROP in rats. a. Schematic diagram illustrated the operation process in the CSE-exposed rats, combined with 3-MA, DFO, and Fer-1 treatment. PBS-treated rats were used as the Control group. b. Three-dimensional reconstruction images of Micro-CT images of rat distal femurs, scale bar:1.0 mm. c. Calculations of bone morphological parameters in the ROI (n = 5). d. 4-HNE IHC staining of rat distal femurs in the Control, CSE, CSE+3-MA, CSE + DFO and CSE + Fer-1 group and statistical analysis of relative AOD of 4-HNE (positive areas were indicated with red arrow) (n = 5), scale bar: 100 μm (round) and 20 μm (square). MDA content assay (e), qPCR analysis of ferroptosis-related genes (Ferritin, NCOA4, GPx4 and PTGS2) (f), WB showing expression level of ferroptosis-related proteins (Ferritin and NCOA4) (g) of rat distal femurs in the Control, CSE, CSE+3-MA, CSE + DFO and CSE + Fer-1 group (n = 5). *P < 0.05, **P < 0.01, ***P < 0.001 versus control. (For interpretation of the references to color in this figure legend, the reader is referred to the Web version of this article.)

observed. Cumulative intake of cigarette smoking was evaluated using the following formula:

Cumulative intake = smoking years × daily intake (picks/day)

4.4. Animals

Specific pathogen free (SPF) male Sprague-Dawley (SD) rats (180–200g, 8 weeks old) for in vivo study and SPF male SD rats (90–120g, 4–5 weeks old) for in vitro study were provided by Experimental Animal Center of Chongqing Medical University (Chongqing, China, license numbers: SCXK(Yu)2012-001). The rats were conditioned in-house for 1 week after arrival with tap water and commercial diet available at will. All the treatments were performed gently and all efforts were made to minimize animal suffering.

For constructing the CSE-exposed rat model, animals were intraperitoneally injected with PBS or CSE at a dose of 1 ml 100%CSE for 250g weight every other day at 4 p.m. as described [42]. Animals were euthanized by CO_2 asphyxiation on day 30. In the pharmacological treatment experiments, Fer-1 was dissolved in mixed solution [1 % DMSO (Solarbio, D8371) + 10 % PEG300 (MCE, HY-Y0873) +5 % Tween-80 (MCE, HY-Y1891) + saline), DFO was dissolved in ddH_2O and 3-MA was dissolved in PBS. Fer-1 (2 mg/kg), DFO (100 mg/kg) or 3-MA (10 mg/kg) was intraperitoneal injection continuously at 10 a.m. for 7 days before CSE exposure and during the CSE treatment process. All animal operations were performed in accordance with the guidelines of for the Care and Use of Laboratory Animals (8th edition, 2011) and were approved by the ethics committee of Chongqing Medical University Affiliated Hospital of Stomatology (*approval number: 2020057*).

4.5. Micro-CT

At the end timepoint, the rat femurs were collected and fixed for 24 h in 4 % paraformaldehyde and were scanned with a micro-CT system (SCANCO, Switzerland) at high resolution using a voxel size of 17.5um, voltage of 70 kV and current of 800 μA. The scanning images were reconstructed to the three-dimensional geometries using N-Recon software for morphometric analysis. Regions of interest (ROI) were defined as 1 mm long cancellous bone trabeculae starting at the end of growth plate of the distal femoral condyles to the direction away from the metaphysis. An upper threshold of 1000 and a lower threshold of 212 was used to delineate each pixel as "bone or non-bone". The calculated indicators of bone morphology parameters included the bone volume/total volume (BV/TV), the trabecular number (Tb.N), the trabecular thickness (Tb.Th), the trabecular separation (Tb.Sp) and BS (bone surface).

4.6. Histological detection

After Micro-CT scanning, the femur samples were rinsed overnight and decalcified in 10 % ethylenediaminetetraacetic acid (EDTA) for 30 days, and then cleared, dehydrated, embedded in paraffin blocks, and sliced at 5 μm. For histological staining, tissue sections were stained with hematoxylin and eosin (H&E, Solabrio, G1120), and Tartrate-resistant acid phosphatase (TRAP, Solabrio, G1492) according to the manufacturers' instruction.

4.7. TUNEL assay

The terminal deoxynucleotidyl transferasemediated dUTP nick end labeling (TUNEL) assay was performed using TUNEL Assay Kits (GDP1042, Servicebio, Wuhan, China) according to manufacturer's instructions. Briefly, after deparaffinization and hydration, antigen repair was performed using proteinase K (20 μg·mL−1) at 37 °C for 25 min, and then permeabilized at room temperature for 20 min. After that, the sections were incubated with TUNEL working solution at 37 °C for 120 min. Finally, the nuclei were stained with 2-(4-Amidinophenyl)-6-indolecarbamidine dihydrochloride (DAPI, Beyotime, C1002) solution for 8 min at room temperature. The TUNEL positive cells were detected using fluorescence microscopy (Nikon DS-U3, Tokyo Japan). The average number of dead cells was assessed by counting of TUNEL positive cells in each high-power field (× 200).

4.8. Immunohistochemistry staining

For immunohistochemistry staining, paraffin slices were treated for deparaffinization and hydration. After pepsin repair and H_2O_2 blocking, the slices were incubated with the primary antibody overnight at 4 °C, and HRP-linked secondary antibody for 1 h at room temperature, followed by 3,3-Diaminobenzidine tetrahy-drochloride (Zhongshan, ZLI-9018) used as a substrate. The nuclei were stained by hematoxylin. Immunohistochemistry was performed using antibodies against 4-HNE (Abcam, 46545, 1:300), Col-1(Proteintech, 66761-1-Ig, 1:300). Images were captured by slice scanner (Leica, Aperio VERSA 8, Germany) and semi-quantitative analyzed by ImageProPlus Software. AOD (average optical density) was calculated as AOD = integrated optical density/area.

4.9. Cell culture

Rat bone marrow mesenchymal stem cells (rBMSCs) were harvested from 4 to 5 weeks old SD rats according to the detailed procedures in previously study [47]. Generally, bone marrow was isolated aseptically by flushing the femurs and tibias of the rats and then suspended in α-MEM culture medium (Hyclone, USA) supplemented with 10 % fetal bovine serum (FBS) (ExCell Bio, China), 1 % penicillin/streptomycin (Hyclone, USA) at 37 °C in a 5 % CO_2 atmosphere. Non-adherent cells were removed after 48h. Medium was changed every 2 days and cells were passaged at 80%–90 % confluence. rBMSCs of passage 3 to passage 6 were employed in the further experiments.

4.10. Measurement of cell viability

Cell viability was determined by CCK-8 assay (MCE, HY-K0301) in vitro. In the rescue experiments, Fer-1 (2μM), DFO (1μM), Nec-1 (10μM), Z-VAD-FMK (10μM), BafA1 (100 nM), RAPA (50 nM), CQ (10 μM), and MitoQ (5 μM) were added in cells 1h before CSE treatment; while 3-MA (20μM) and NAC (2 mM) were added simultaneously with CSE. In the siRNA knockdown experiment, rBMSCs were transfected with siRNA for 36h and then treated with CSE, and CCK-8 assay was performed at designated time. The absorbency of the solution was measured on a microplate reader at 450 nm (PerkinElmer, America).

The relative cytotoxicity rate was evaluated using the following formula:

$$\text{Viability } (\%) = (A_{\text{experiment group}}\text{-}A_{\text{blank group}}) / (A_{\text{control group}}\text{ -}A_{\text{blank group}}) \times 100\%$$

4.11. Detection of lactate dehydrogenase (LDH) in cell culture medium

According to the instruction of LDH assay kit (Beyotime, C0016), we use LDH releasing reagent to detected LDH enzyme activity of cells and collected the LDH of rBMSCs in different treatment by adding the LDH working solution. After 30min of incubation at room temperature away from light, the absorbance was read at 490 nm (PerkinElmer, America).

$$\text{Cytotoxicity } (\%) = (A_{\text{treatment group}}\text{-}A_{\text{control group}}) / (A_{\text{maximum enzyme activity}}\text{ -}A_{\text{control group}}) \times 100\%$$

4.12. In vitro osteoblastic differentiation

For osteoblastic differentiation, rBMSCs were seeded in a 24-well microplate at a density of 5×10^4 per well, and were switched to osteogenic differentiation induction medium (OM) containing α-MEM culture medium, 10 % FBS, 10 nM dexamethasone (Sigma, D2915), 10 mM β-glycerolphosphate (Sigma, G6251), and 50 μM L-ascorbic acid (Sigma, 4403). After 7 days of culture, RNA was collected to detected to the expression of osteogenic differentiation genes. After 14 days of culture, cells were fixed with 4 % paraformaldehyde and then stained with 1 % alizarin red (Solarbio, G1452) for 5min. The whole-well images were captured with a camera (Nikon, D100, Japan) and microscopy images were obtained by optical microscopy (Olympus, IX73, Japan).

4.13. In vitro adipogenic differentiation

For adipogenic differentiation, rBMSCs were cultured in induction medium as the manufactory demand (Cyagen, RAXMX-90031). After 6 days of culture, RNA was collected to detected to the expression of adipogenic differentiation genes. After 21 days of culture, cells were fixed with 4 % paraformaldehyde and then stained with Oil Red O. Microscopy images were obtained by optical microscopy (Olympus, IX73, Japan).

4.14. In vitro osteoclast differentiation

For osteoclast differentiation, rat bone marrow mononuclear macrophages (rBMMs) were isolated from rat femur and were cultured in α-MEM containing 10 % fetal bovine serum (FBS) in a humidified incubator at 37 °C and 5 % CO2 in the presence of Monocyte colony stimulating factor (MCSF) and Receptor activator of nuclear factor kappa-B ligand (RANKL). M-CSF (C470) and RANKL (CR06) were purchased from Novoprotein (China). After two days of osteoclast differentiation, RNA was collected to detected to the expression of osteoclast differentiation genes. After 6 days of culture, cells were fixed with 4 % paraformaldehyde and then stained with TRAP (Solarbio, G1492) working solution. Microscopy images were obtained by optical microscopy (Olympus, IX73, Japan).

4.15. Measurement of lipid peroxidation in vitro

rBMSCs were seeded in a 96-well microplate at a density of 5×10^3 per well. Lipid peroxidation was measured using a C11-BODIPY 581/591 probe (Invitrogen, C10445) as the manufacturers' demands. Briefly, cells were incubated for 30 min with C11-BODIPY 581/591 (5μM) in FBS-free culture medium. Images were captured by a fluorescence microscope (EVOS FL Auto, Invitrogen, USA). Fluorescence intensity of C-11 BODIPY probe was measured by acquisition of the green signals (484/510 nm) and red signals (581/610 nm) (CLARIOstar®, BMG LABTECH, USA). The fluorescence shifts from red to green in response to oxidation, and the fluorescence ratio of green light to red light presents indication of lipid peroxidation.

4.16. Measurement of GSH

Total glutathione in cell lysates or tissue lysates were measured with GSH detection kit (Beyotime, S0052) according to the manufacturer's instruction.

4.17. Measurement of MDA

The tissue lysates were measured with MDA detection kit (Beyotime, S0131) according to the manufacturer's instruction.

4.18. Flow cytometry

TMRE (10 nM) was used to measure mitochondrial membrane potential, PGSK (5 μM) was used to detect intracellular iron and MitoSox (5 μM) was used to evaluated mitochondrial ROS. Briefly, at the end timepoint of culturing, rBMSCs were trypsinization, washed twice with PBS and then stained with TMRE (10 nM), PGSK (5 μM) or MitoSox (5 μM) for 20 min at 37 °C. After washing twice with PBS and resuspending with 100ul PBS containing 1%FBS. All samples were performed on BD Influx Cell Sorter (BD Biosciences, San Jose, CA, USA) and results were analyzed using the FlowJo Software.

4.19. Intracellular ROS and mitochondrial ROS measurement

For intracellular ROS staining, the fluorescent probe DCFH-DA was used. Briefly, the cells were incubated with DCFH-DA (10 μM) in PBS for 30 min in the dark. After rinsing with PBS three times, the cells were observed under a fluorescence microscope. For mitochondrial ROS, the cells were incubated with MitoSox (1 μM) diluted in serum-free culture medium for 20 min in the dark. After rinsing with PBS three times, the cells were observed under confocal microscope (Leica TCS SP8, Germany).

4.20. Iron assay

The labile iron pool of rBMSCs was measured with Intracellular Iron Colorimetric Assay Kit (Applygen, E1042) according to the manufacturer's instruction. Meanwhile, total protein quantification was determined by the BCA Assay Kit (Beyotime, P0009).

4.21. Transcriptomic analysis

Passage 3 rBMSCs were cultured in complete growth medium to 80 % confluence and treated with 3%CSE or PBS for 6h. Cells were harvested and total RNA was prepared using RNAiso Plus Lysate (Takara, Japan) for RNA-sequence analysis (Novelbio, Shanghai, China). Differentially expressed genes (DEGs) were determined by DESeq2 (Fold change >2; FDR<0.05). The annotated DEGs were analyzed using Database for Annotation, Visualization, and Integrated Discovery (DAVID) (https://david.ncifcrf.gov/) based on Gene Ontology (GO) and Kyoto Encyclopedia of Genes and Genomes (KEGG) analysis. Gene set enrichment analysis (GSEA) was used to evaluate DEGs enriched for either negatively or positively correlated gene. $P < 0.05$ was considered to indicate a significant difference. The RNA-Sequence data were deposited in the NCBI GEO database with accession code GSE206079.

4.22. Total RNA preparation and quantitative RT-PCR analysis

Total RNA was extracted from rBMSCs using RNAiso Plus Lysate

(Takara, Japan), while total RNA of rat femur was extracted according to the manufacturers' instruction (Beyotime, R0026). Reverse transcription was performed for synthesis of cDNA by using PrimeScript Master Mix (TaKaRa), and quantitative RT-PCR (qPCR) was performed using TB Green Premix Ex Taq II (TaKaRa) on CFX96 Touch Real-Time PCR Detection System (Bio-Rad, Hercules, CA, USA). The relative gene expression levels were calculated using the CT value and normalized to the expression of β-actin reference genes. The detailed sequences were listed in Table 1 in supporting information.

4.23. Co-immunoprecipitation and western blot

rBMSCs after being washed twice with cold PBS were treated with ice-cold IP lysis buffer (CST, 9803S) containing Phenylmethanesulfonyl fluoride (PMSF, Sigma, 36978) and protease inhibitors (Aprotinin, Sigma, A1153; Leupeptin hydrochloride, Sigma, L0649; Pepstatin A, Sigma, P4265; Na_3VO_4, Sigma, 450243; NaF, Sigma, 450022). The protein concentrations of cell lysates were determined by the BCA Assay Kit. 500ug total protein lysates from each sample were immunoprecipitated with 25 μl resuspended volume of Dynabeads™ Protein G (Invitrogen, 10003D) pre-treated with 2.5ul rabbit polyclonal IgG control antibody or Ferritin Rabbit mAb (CST, 4393) at room temperature for 1h at 4 °C overnight. After washing and denaturing with Dynabeads, the eluted proteins were subjected to polyacrylamide gel electrophoresis and analyzed by western blot.

For western blot (WB) analysis, rBMSCs or rat femur were treated with ice-cold RIPA lysis buffer with PMSF and protease inhibitors as mentioned above. 30ug protein from each sample were separated via SDS-PAGE and transferred onto polyvinylidene difluoride (PVDF) films (bore diameter = 0.22μm). The PVDF films were blocked with 5 % nonfat dry milk (Cell Signaling Technology, #9999) and then probed separately with the corresponding primary overnight at 4 °C and horseradish peroxidase-linked secondary antibodies for 2h at room temperature. Bands were developed with enhanced chemiluminescent imaging system (Bio-rad, USA) and band relative density was calculated by ImageJ (NIH Image, USA).

The primary antibodies used in this study were listed below: GPx4 (ab125066, 1:1000), Ferritin (ab183781, 1:1000) were obtained from Abcam; LC3A/B (12741, 1:1000), p62 (23214, 1:1000), p62 (5114, 1:1000), ATG5 (12994, 1:1000), Phospho-mTOR (Ser2448) (5536, 1:1000), MTOR (2983; 1:1,000), phospho-PRKAA/AMPK (Thr172) (2535, 1:1000), PRKAA/AMPK (5832; 1:1000), phospho-ULK1 (Ser555; 5869; 1:1,000), ULK1 (8054, 1:1000) were purchased from Cell Signaling Technology; NCOA4 (sc-373739; 1:150) and Ferritin heavy chain (sc-376594; 1:150) were purchased from Santa Cruz Biotechnology; β-actin (66009-1-Ig, 1:3000), mouse secondary antibodies (SA00001-1, 1:6000) and rabbit secondary antibodies (SA00001-2, 1:6000) were obtained from Proteintech; Slc7a11 (A2413, 1:1000) were purchased from ABclonal.

4.24. Transmission electron microscopy (TEM) assays

CSE-exposed or PBS-treated rBMSCs were centrifuged at 1200 g for 20 min after trypsinization and fixed with 4 % glutaraldehyde for 24h at 4 °C. Then, cells were fixed with 1 % osmium tetroxide for 1 h at 4 °C. Subsequently, cells were dehydrated in a graded series of alcohol and acetone, followed by embedment in Epon 816 (Electron Microscopy Sciences, Hatfield, PA, USA). Ultrathin sections were obtained by using a Leica ultramicrotome (Leica Microsystems, Buffalo Grove, IL, USA) and stained with uranyl acetate and lead citrate. TEM images were captured under a JEM-1400Plus transmission electron microscope (JEOL Ltd. Tokyo, Japan).

4.25. Adenoviral infection

Adenoviral mRFP-GFP-LC3 (Hanbio, Wuhan, China) was used to transfect rBMSCs to indicate autophagy flux. rBMSCs were cultured in 24-well plates and infected with adenoviral mRFP-GFP-LC3 at a cell density of 50 %. Medium was refreshed after 8h, and the cells were cultured for a further 48h. Cells were treated by CSE or/and CQ. Before observation, rBMSCs were washed with PBS and fixed for 10 min with 4 % paraformaldehyde. The nuclei were stained with DAPI (Beyotime, C1002). The mRFP-GFP-LC3 dot formation was visualized by confocal microscope. Autophagic flux was measured by counting the cells with $mRFP^+/GFP^+$ (yellow) and $mRFP^+/GFP^-$ (red) dots by Image J software (NIH Image, USA) based on the high-resolution fluorescence confocal images. 6 cells were counted per sample in triplicate experiments.

4.26. siRNA transfection

rBMSCs were seeded in 24-well plates and transfected with siRNA duplexes (50 nM) with PepMute™ siRNA Transfection Reagent (SignaGen, SL100566, USA) diluted in PepMute™ Transfection Buffer (SignaGen, SL100575, USA) according to the manufacturer's instructions. The efficiency of knockdown was determined by qPCR after 24h of transfection. At 48h, rBMSCs were treated with CSE. After that, WB analysis, CCK-8 assay, and lipid peroxidation detection were carried out at designated time. SiRNAs used in this study were synthesized by Tsingke (Beijing, China), and the sequences were listed in Table 2 in supporting information. Negative control (NC) sequence was offered from Tsingke Biotechnology Corporation.

4.27. Immunofluorescence staining

rBMSCs seeded on coverslips were fixed with 4 % paraformaldehyde for 10 min at room temperature and subsequently permeabilized with 0.1 % Triton X-100 (Sigma, X100) and then blocked with 5 % donkey serum (Jackson, USA) for 60 min for 1 h at room temperature. Cells were incubated with primary antibodies including LC3B (CST, 83506, 1:250) and Ferritin (CST, 4393, 1:250) overnight at 4 °C and with fluorochrome-conjugated secondary antibodies (Invitrogen, R37114, 1:300; Invitrogen, A-31573, 1:300) for 1 h at room temperature away from light. At the end, the nuclei were labeled with DAPI (Beyotime, C1002, 1:2000) for 2 min at room temperature. Cells were washed three times with PBS, and the coverslips were sealed with antifade mounting medium (Beyotime, P0126). Fluorescence images were acquired using confocal microscope. Plotting of the plot profile curves were done using Image J Software and GraphPad Software.

4.28. Statistical analysis

For comparison between the two groups, two tailed Student's t-test analysis was performed. When comparing more than two groups, One-way analysis of variances (ANOVA) with Tukey's post hoc test was conducted. Data were shown as the mean ± standard deviation (S.D.), with $*P < 0.05$ considered significant, $**P < 0.01$ and $***P < 0.001$ considered as higher significant, and ns. indicating not significant. All statistical tests were conducted using Prism 8.0 software (GraphPad Software, San Diego, CA, USA). At least three independent experiments were performed in this study.

Disclosure statement

The authors declare that they have no competing financial interests. Figures in the study were created with BioRender software (https://biorender.com), (accessed on Sep 5th, 2023).

Funding

This work was supported by National Natural Science Foundation of China (Grant No. 82171010, 82270962, 82071115, 82001103, 82370973); the Natural Science Foundation of Chongqing, China (Grant

No. cstc2021jcyj-jqX0028, cstc2020jcyj-msxmX0131); CQMU Program for Youth Innovation in Future Medicine (No. W0079); Project of Chongqing Medical University Graduate Tutor Team (dstd202203).

Declaration of competing interest

The authors declare that they have no competing financial interests.

Data availability

Data will be made available on request.

Acknowledgements

We apologize to the researchers who were not referenced due to space limitations, and sincerely appreciate everyone's efforts for this study. Sheng Yang and Yuzhou Li were responsible for project design. Sheng Yang and Ping Ji provided funding support and supervised the research. Zheng Jing, Jinrui Yu, Kai Xiang, Xuerui Gong worked for in vivo experiments. Zheng Jing, Tao Chen and Xinxin Xu work for the in vitro experiments. Yuzhou Li and He Zhang analyzed the data and transcriptomic test. Ping He and Xu Wang organized images. Zheng Jing and Yulong Zou collected the clinical data. Zheng Jing wrote the manuscript. Mingxing Ren and Yiru Fu help to revise the manuscript.

Appendix A. Supplementary data

Supplementary data to this article can be found online at https://doi.org/10.1016/j.redox.2023.102922.

References

[1] K.A. Hollenbach, et al., Cigarette smoking and bone mineral density in older men and women, Am. J. Publ. Health 83 (1993) 1265–1270, https://doi.org/10.2105/ajph.83.9.1265.
[2] P. Egger, et al., Cigarette smoking and bone mineral density in the elderly, J. Epidemiol. Community Health 50 (1996) 47–50, https://doi.org/10.1136/jech.50.1.47.
[3] J.A. Kanis, et al., Smoking and fracture risk: a meta-analysis, Osteoporos. Int. 16 (2005) 155–162, https://doi.org/10.1007/s00198-004-1640-3.
[4] World Health Organization, Tobacco, WHO, 2022. https://www.who.int/news-room/fact-sheets/detail/tobacco.
[5] G.R.B. Saunders, et al., Genetic diversity fuels gene discovery for tobacco and alcohol use, Nature 612 (2022) 1476–4687, https://doi.org/10.1038/s41586-022-05477-4.
[6] C.H. Ko, et al., Deteriorating effect on bone metabolism and microstructure by passive cigarette smoking through dual actions on osteoblast and osteoclast, Calcif. Tissue Int. 96 (2015) 389–400, https://doi.org/10.1007/s00223-015-9966-8.
[7] A.M. Al-Bashaireh, et al., The effect of tobacco smoking on bone mass: an overview of pathophysiologic mechanisms, J. Osteoporos. 2018 (2018) 1206235, https://doi.org/10.1155/2018/1206235.
[8] T. Sözen, et al., An overview and management of osteoporosis, Eur. J. Rheumatol. 4 (2017) 46–56, https://doi.org/10.5152/eurjrheum.2016.048.
[9] W. Liu, et al., Abnormal inhibition of osteoclastogenesis by mesenchymal stem cells through the miR-4284/CXCL5 axis in ankylosing spondylitis, Cell Death Dis 10 (2019) 188, https://doi.org/10.1038/s41419-019-1448-x.
[10] T. Nyunoya, et al., Cigarette smoke induces cellular senescence, Am. J. Respir. Cell Mol. Biol. 35 (2006) 681–688, https://doi.org/10.1165/rcmb.2006-0169OC.
[11] B. Messner, et al., Apoptosis and necrosis: two different outcomes of cigarette smoke condensate-induced endothelial cell death, Cell Death Dis 3 (2012) e424, https://doi.org/10.1038/cddis.2012.162.
[12] W.Z. Zhang, et al., Smoking-induced iron dysregulation in the lung, Free Radic. Biol. Med. 133 (2019) 238–247, https://doi.org/10.1016/j.freeradbiomed.2018.07.024.
[13] Y.S. Lin, et al., Cigarette smoking, cadmium exposure, and zinc intake on obstructive lung disorder, Respir. Res. 11 (2010) 53, https://doi.org/10.1186/1465-9921-11-53.
[14] E. Balogh, et al., Influence of iron on bone homeostasis, Pharmaceuticals 11 (2018) 107, https://doi.org/10.3390/ph11040107.
[15] M.R. Sepand, et al., Cigarette smoke-induced toxicity consequences of intracellular iron dysregulation and ferroptosis, Life Sci 281 (2021) 119799, https://doi.org/10.1016/j.lfs.2021.119799.
[16] A.J. Ghio, et al., Particulate matter in cigarette smoke alters iron homeostasis to produce a biological effect, Am. J. Respir. Crit. Care Med. 178 (2008) 1130–1138, https://doi.org/10.1164/rccm.200802-334OC.
[17] J.J. Moreno, et al., Release of iron from ferritin by aqueous extracts of cigarette smoke, Chem. Res. Toxicol. 5 (1992) 116–123, https://doi.org/10.1021/tx00025a020.
[18] M. Yoshida, et al., Involvement of cigarette smoke-induced epithelial cell ferroptosis in COPD pathogenesis, Nat. Commun. 10 (2019) 3145, https://doi.org/10.1038/s41467-019-10991-7.
[19] W. Hou, et al., Autophagy promotes ferroptosis by degradation of ferritin, Autophagy 12 (2016) 1425–1428, https://doi.org/10.1080/15548627.2016.1187366.
[20] M. Buccarelli, et al., Inhibition of autophagy increases susceptibility of glioblastoma stem cells to temozolomide by igniting ferroptosis, Cell Death Dis 9 (2018) 841, https://doi.org/10.1038/s41419-018-0864-7.
[21] W.E. Dowdle, et al., Selective VPS34 inhibitor blocks autophagy and uncovers a role for NCOA4 in ferritin degradation and iron homeostasis in vivo, Nat. Cell Biol. 16 (2014) 1069–1079, https://doi.org/10.1038/ncb3053.
[22] R. Bellelli, et al., NCOA4 deficiency impairs systemic iron homeostasis, Cell Rep 14 (2016) 411–421, https://doi.org/10.1016/j.celrep.2015.12.065.
[23] J. Kim, et al., AMPK and mTOR regulate autophagy through direct phosphorylation of Ulk1, Nat. Cell Biol. 13 (2011) 132–141, https://doi.org/10.1038/ncb2152.
[24] M. Holczer, et al., A double negative feedback loop between mTORC1 and AMPK kinases guarantees precise autophagy induction upon cellular stress, Int. J. Mol. Sci. 20 (2019) 5543, https://doi.org/10.3390/ijms20225543.
[25] S. Herzig, et al., AMPK: guardian of metabolism and mitochondrial homeostasis, Nat. Rev. Mol. Cell Biol. 19 (2018) 121–135, https://doi.org/10.1038/nrm.2017.95.
[26] B. Gan, Mitochondrial regulation of ferroptosis, J. Cell Biol. 220 (2021), e202105043, https://doi.org/10.1083/jcb.202105043.
[27] H. Wang, et al., Mitochondria regulation in ferroptosis, Eur. J. Cell Biol. 99 (2020) 151058, https://doi.org/10.1016/j.ejcb.2019.151058.
[28] S.J. Dixon, et al., Ferroptosis: an iron-dependent form of nonapoptotic cell death, Cell 149 (2012) 1060–1072, https://doi.org/10.1016/j.cell.2012.03.042.
[29] P. Liu, et al., Ferroptosis: a new regulatory mechanism in osteoporosis, Oxid. Med. Cell. Longev. 2022 (2022) 2634431, https://doi.org/10.1155/2022/2634431.
[30] B.R. Stockwell, et al., Ferroptosis turns 10: emerging mechanisms, physiological functions, and therapeutic applications, Cell 185 (2022) 2401–2421, https://doi.org/10.1016/j.cell.2022.06.003.
[31] M. Sato, et al., The ferroptosis inducer erastin irreversibly inhibits system xc− and synergizes with cisplatin to increase cisplatin's cytotoxicity in cancer cells, Sci. Rep. 8 (2018) 968, https://doi.org/10.1038/s41598-018-19213-4.
[32] M. Gao, et al., Ferroptosis is an autophagic cell death process, Cell Res 26 (2016) 1021–1032, https://doi.org/10.1038/cr.2016.95.
[33] J.P. Friedmann Angeli, et al., Inactivation of the ferroptosis regulator Gpx4 triggers acute renal failure in mice, Nat. Cell Biol. 16 (2014) 1180–1191, https://doi.org/10.1038/ncb3064.
[34] Y. Du, et al., Evaluating the correlations between osteoporosis and lifestyle-related factors using transcriptome-wide association study, Calcif. Tissue Int. 106 (2020) 256–263, https://doi.org/10.1007/s00223-019-00640-y.
[35] J.D. Mancias, et al., Quantitative proteomics identifies NCOA4 as the cargo receptor mediating ferritinophagy, Nature 509 (2014) 105–109, https://doi.org/10.1038/nature13148.
[36] X. Chen, et al., Cellular degradation systems in ferroptosis, Cell Death Differ 28 (2021) 1135–1148, https://doi.org/10.1038/s41418-020-00728-1.
[37] B. Chen, et al., Gut bacteria alleviate smoking-related NASH by degrading gut nicotine, Nature 610 (2022) 562–568, https://doi.org/10.1038/s41586-022-05299-4.
[38] X. Qin, et al., Ferritinophagy is involved in the zinc oxide nanoparticles-induced ferroptosis of vascular endothelial cells, Autophagy 17 (2021) 4266–4285, https://doi.org/10.1080/15548627.2021.1911016.
[39] M. Gao, et al., Role of mitochondria in ferroptosis, Mol. Cell 73 (2019) 354–363. e353, https://doi.org/10.1016/j.molcel.2018.10.042.
[40] H. Lee, et al., Energy-stress-mediated AMPK activation inhibits ferroptosis, Nat. Cell Biol. 22 (2020) 225–234, https://doi.org/10.1038/s41556-020-0461-8.
[41] F. Javed, et al., Tobacco-product usage as a risk factor for dental implants, Periodontol 2000 81 (2019) 48–56, https://doi.org/10.1111/prd.12282.
[42] G. Cyprus, et al., Cigarette smoke increases pro-inflammatory markers and inhibits osteogenic differentiation in experimental exposure model, Acta Biomater 76 (2018) 308–318, https://doi.org/10.1016/j.actbio.2018.06.018.
[43] H. Guo, et al., Maqui berry and ginseng extracts reduce cigarette smoke-induced cell injury in a 3D bone Co-culture model, Antioxidants 11 (2022), https://doi.org/10.3390/antiox11122460.
[44] S. Zhu, et al., Maqui berry extract prevents cigarette smoke induced oxidative stress in human osteoblasts in vitro, EXCLI J 20 (2021) 281–296, https://doi.org/10.17179/excli2020-3244.
[45] G. Aedo, et al., A reliable preclinical model to study the impact of cigarette smoke in development and disease, Curr. Protoc. Toxicol. 80 (2019) e78, https://doi.org/10.1002/cptx.78.
[46] K.F. Braun, et al., Quercetin protects primary human osteoblasts exposed to cigarette smoke through activation of the antioxidative enzymes HO-1 and SOD-1, Sci. World J. 11 (2011) 2348–2357, https://doi.org/10.1100/2011/471426.
[47] Z. Jing, et al., Carbon nanotube reinforced collagen/hydroxyapatite scaffolds improve bone tissue formation in vitro and in vivo, Ann. Biomed. Eng. 45 (2017) 2075–2087, https://doi.org/10.1007/s10439-017-1866-9.